Accepted Manuscript

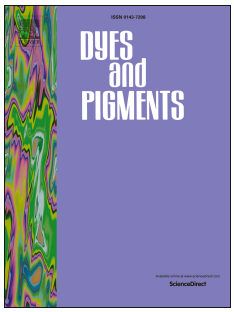

Influence of temperature and dopant concentration on structural, morphological and optical properties of nanometric $Ce_{1-x}Er_xO_{2-\delta}$ (x = 0.05–0.20) as a pigment

Marija Stojmenović, Maja C. Milenković, Predrag T. Banković, Milan Žunić, Jelena J. Gulicovski, Jelena R. Pantić, Snežana B. Bošković

PII: S0143-7208(15)00298-3

DOI: 10.1016/j.dyepig.2015.07.030

Reference: DYPI 4870

To appear in: *Dyes and Pigments*

Received Date: 12 March 2015

Revised Date: 19 June 2015

Accepted Date: 23 July 2015

Please cite this article as: Stojmenović M, Milenković MC, Banković PT, Žunić M, Gulicovski JJ, Pantić JR, Bošković SB, Influence of temperature and dopant concentration on structural, morphological and optical properties of nanometric $Ce_{1-x}Er_xO_{2-\delta}$ (x = 0.05–0.20) as a pigment, *Dyes and Pigments* (2015), doi: 10.1016/j.dyepig.2015.07.030.

Influence of temperature and dopant concentration on structural, morphological and optical properties of nanometric $Ce_{1-x}Er_xO_{2-\delta}$ (x = 0.05–0.20) as a pigment

Marija Stojmenović[a,*], Maja C. Milenković[b], Predrag T. Banković[c], Milan Žunić[d], Jelena J. Gulicovski[a], Jelena R. Pantić[a], Snežana B. Bošković[a]

[a]University of Belgrade–Institute of Nuclear Sciences Vinča, Mike Petrovića Alasa 12–14, Belgrade, Serbia

[b]University of Belgrade–Faculty of Physical Chemistry, Studentski trg 12, 11000 Belgrade, Serbia

[c]University of Belgrade–Institute of Chemistry, Technology and Metallurgy–Center for Catalysis and Chemical Engineering, Njegoševa 12, 11000 Belgrade, Serbia

[d]Physical Sciences and Engineering Division, King Abdullah University of Science and Technology (KAUST), Thuwal 23955–6900, Saudi Arabia

Abstract

Ceramic pigments based on cerium oxide were synthesized by self–propagating room temperature method and their color properties were assessed from the viewpoint of potential environmentally nontoxic pink pigments. Thermal stabilities of the pigments were examined at 600, 900 and 1200 ºC. According to X–ray powder diffraction and Raman spectroscopy results, all obtained pigments were single–phase solid solutions of cerium oxide, independent of the concentration of dopants. The X–ray analysis showed that the crystallites were of nanometric dimensions, as recorded and by transmission electron microscopy analysis. Color characteristics of solid solutions, which depended on concentracion erbium ions and calcination temperature,

* Corresponding author: Marija Stojmenović
Tel.: +381 11 340 8860; fax: +381 11 340 8224.
E–mail address: mpusevac@vinca.rs

and their position in the chromaticity diagram were studied by ultraviolet–visible spectrophotometry, which confirmed potential application of environmentally friendly pigments of desired color. The color efficiency of pigments was also evaluated by colorimetric analysis.

Keywords: Rare earth pigments, Non–toxic pigments, Optical properties, Band gap, Colorimetric

1. Introduction

In past few years lanthanide ions have attracted great attention due to their unique optical properties and specific functions make them useful in a wide range of industrial applications. The areas of application included tunable lasers, amplifiers for optical communications, organic light–emitting diodes and inorganic pigments [1–5]. Inorganic pigments are also used for various applications such as paints, ceramics, inks, plastics, rubbers and glasses [6, 7]. The use of pigments is not only due to their coloristic properties. They also protect the coating from the effects of solar light (UV, VIS and IC light). In order to be suitable in a wide variety of applications, they need to possess high thermal and color stability. The majority of inorganic pigments, which are currently employed on an industrial scale, generally, comprise toxic metals, such as Cr, Co, Ni, Se, Cd, and Pb [8, 9], which are harmful not only to human health but also to the environment. Because of their high toxicity, the use of the above pigments in many countries has increasingly been becoming the subject of strict control regulated by government legislation and regulations. At present, the following classical pigments used on a large scale are: iron oxide (Fe_2O_3) encapsulated in zircon ($ZrSiO_4$) matrix and lead oxide (Pb_3O_4) in tin oxide (SnO_2) matrix give pale red or pink colors [10]. The red–orange pigments in the $Cd(S_xSe_{1-x})$–$ZrSiO_4$ system, and sodium urinate are toxic and unstable above 900 ºC [11].

Today, in order to solve the problems of toxicity and instability of pigments, there is a great interest in the development of nanosized ceramic pigments based on CeO_2. Namely, CeO_2 and its related pigments have been attracting much attention recently because of their high thermal and chemical stability [12, 13], as well as their ability to filter ultraviolet (UV) radiation [14, 15]. The study on the production of red ceramic pigments with high thermal stability is of great importance to the industry [16]. One way to obtain red pigments is the doping of ceria (CeO_2) with praseodymium (Pr^{4+}) ions, which is the method that yields a stable dye [17–19]. The production of ceramics pigments is focused towards obtaining high surface area pigments in the form of powder, since this feature influences the color intensities. Furthermore, there are a number of processes to prepare and modify CeO_2 fine particles [20, 21]. It is reported that one can control the color hue of pigments by the incorporation of another element into the CeO_2 lattice, because the coloring mechanism is based on the charge transfer transition from O_{2p} to Ce_{4f} in the CeO_2 band structure, which can be modified by the introduction of an additional electronic level between the anionic O_{2p} valence band and the cationic Ce_{4f} conduction band [9].

Different chemical methods can be used for the synthesis of pure or doped CeO_2. Among them, the electrochemical deposition method [22], hydrothermal synthesis [23–25], pyrrolidone solution route [26, 27], sol–gel method [28, 29], soft solution method [30–32], co–precipitation technique [33, 34], modified glycine–nitrate procedure [35] and self–propagating reaction at room temperature [35] can all be listed.

Among the above mentioned processes available for the synthesis of nanometric ceramic powders, the self–propagating reaction at room temperature (SPRT method) is the most promising because of a number of advantages over conventional methods [36–38]. Therefore, the SPRT method was applied in this work for the synthesis of Er^{3+} doped ceria powders ($Ce_{1-x}Er_xO_{2-\delta}$; x = 0.05–0.20), where δ denotes oxygen deficiency, i.e., departure from stoichiometry, both due

to introduction of dopant cations (x), and due to intrinsic nonstoichiometry. The SPRT procedure is based on the self–propagating room temperature reaction between metal nitrates and sodium hydroxide, wherein the reaction is spontaneous and terminates extremely fast. The method is known to assure very precise stoichiometry of the final product in comparison with a tailored composition. Moreover, the SPRT method is very fast and reliable, whereby the required equipment is extremely simple and inexpensive.

As a good candidate for obtaining ceramic pigments based on CeO_2 the various shades of pink color was chosen erbium ion (Er^{3+}), because of its lower valence state than ceria and pink color, which enables the coloring of the different oxides and glass [39–42]. Furthermore, there is a lack of literature data about Er^{3+} as a dopant ion in ceria solid solution. CeO_2 doped with different ions and in different concentrations [12–21, 43], as a novel class of potential environment–friendly pigments, enables obtaining of ceramic pigments with different colors and shades.

Thus, the present paper is focused on the synthesis of Er^{3+} doped CeO_2 ($Ce_{1-x}Er_xO_{2-\delta}$; x = 0.05–0.20), as a novel class of potential environment–friendly ceramic pink pigment, by using the self–propagating reaction at room temperature. Apart from the interest to get more fundamental knowledge on the characteristics of solid solutions under study, of great interest is the study of their structural, morphological and optical properties after thermal treatment at 600, 900 and 1200 ºC for 4 h in air (for the potential application in industrial production), which is also presented in this work.

2. Experimental procedure

2.1. Materials and method

SPRT procedure is based on the self–propagating room temperature reaction between metal nitrates and sodium hydroxide, wherein the reaction is spontaneous and terminates extremely fast [35]. Starting reactants for the synthesis of powders of doped ceria $Ce_{1-x}Er_xO_{2-\delta}$ (x = 0.05–0.20) were Ce and Er nitrates (Aldrich, USA), and NaOH (Vetprom–Chemicals). The quantities of reactants needed for the synthesis of doped CeO_2 nanopowders were calculated via reaction (1):

$$(1-x)Ce(NO_3)_3{\cdot}6H_2O + xEr(NO_3)_3{\cdot}5H_2O + 3NaOH + (1/2-\delta)O_2 \rightarrow$$
$$\rightarrow Ce_{1-x}Er_xO_{2-\delta} + 3NaNO_3 + yH_2O \quad (1)$$

Mechanochemical synthesis of doped CeO_2 nanopowders was carried out in an alumina mortar by mixing reactants for 15 minutes. The presence of air in the period of 3 hours provided total termination of reaction according to the reaction (1). Entire quantity of powder was dispersed in water and centrifuged for 10 minutes in a Centurion 102 D 3000 rpm centrifuge. Powder washing was repeated four times with distilled water and two times with ethanol. After this process $NaNO_3$ from the synthesized powder was completely removed. This was confirmed after the analysis of the powder on Na content by titration with EDTA. The obtained nanopowders were dried at 100 ºC. In this manner ethanol was removed by evaporation. After drying, a part of powder was heat treated at 600, 900 and 1200 ºC for 4 h in air.

2.2. Instruments

With the aim to compare properties of synthesized nanopowders $Ce_{1-x}Er_xO_{2-\delta}$ (x = 0.05–0.20), the characterization of powders obtained at room temperature (25 ºC) [44], and those calcined at 600, 900 and 1200 ºC was performed. The characterization techniques included X–ray powder

diffraction (XRPD), transmission electron microscopy (TEM), scanning electron microscopy (SEM), Fourier transform infrared spectroscopy (FTIR), Raman spectroscopy, and diffuse reflectance (DR) spectroscopy in the ultraviolet (UV) and visible (VIS) region.

All powders were characterized at room temperature by X–ray powder diffraction (XRPD) using an Ultima IV Rigaku diffractometer, equipped with Cu Kα1,2 radiation, applying generator voltage of 40.0 kV and generator current of 40.0 mA. The range of 20–80 º 2θ was used for all samples in a continuous scan mode with the step of 0.02 º and at the scan rate of 2 º/min. Before measurement, the angular correction was performed by means of a high quality Si standard. Lattice parameters (a_{XRPD}) were refined using the least square procedure. Standard deviation was about 1 %. The microstrain ($e_{XRPD}=\Delta d/d$) was estimated from the Williamson–Hall plots based on the following equation [45]:

$$\beta_{total} \cdot \cos\theta = 0.9\lambda/D_{XRPD} + 4(\Delta d/d) \cdot \sin\theta \quad (2)$$

where β_{total} is the full width half maximum of the XRPD peak, λ is the incident X–ray wavelength, θ is the diffraction angle, D_{XRPD} is the crystallite size and Δd is the difference of the d spacing corresponding to a typical peak.

Raman spectra were collected on a DXR Raman microscope (Thermo Scientific, USA), equipped with a diode pumped solid state high–brightness laser (λ=532 nm) as the source of incident light, an Olympus optical microscope and a CCD detector. The measurements were made at room temperature in the spectral range from 200–800 cm^{-1}. The powdered sample was placed on X–Y motorized sample stage. Laser beam was focused on the sample using the

objective magnification of 10×. Scattered light was analyzed by a spectrograph with a diffraction grating 900 lines/mm. Laser power was kept at 1 mW.

Transmission electron microscopy (TEM) analysis of obtained powders and their particles size was measured by TEM–ZEISS EM 912 Omega. Particle size was measured on micrographs directly after they had been taken using the existing computer Digital Micrograph software. The micrographs with as much as possible isolated particles were chosen for measurements. Diameter of the particles was measured manually, on computer, and this result was recalculated by Digital micrograph software into particles size. Approximately 40 particles were measured for each sample. The mean value was taken as the particle size of the relevant powder.

Microstructures of the synthesized samples were observed using the scanning electron microscopy (SEM) analysis (TESCAN Vega TS5130MM). The samples were pre–coated with a several nanometers thick layer of gold before observation. A Fine Coat JFC–1100 ION SPUTTER Company JEOL device was used for the coating procedure. The EDS analysis was carried out at the invasive electron energy of 30 keV by means of QX 2000S device by Oxford Microanalysis Group. The maximum resolution was 0.4 nm.

Fourier transform infrared (FTIR) spectra of the samples before and after the calcination were collected using a PerkinElmer Spectrum Two FT–IR spectrometer in the transmission mode using pressed KBr pellets (1:100) technique in the 450–4000 cm^{-1} range with the resolution of 4 cm^{-1}.

The optical properties of all samples were analyzed by diffuse reflectance (DR) spectroscopy in ultraviolet (UV) and visible (VIS) region. Spectra were recorded using a Thermo Electron Nicolet Evolution 500 UV–VIS spectrophotometer equipped with an RSA–UC–40 diffuse reflectance accessory. A Labsphere USRS–99–010 was used as a reflectance standard.

The color characteristics of specimens were calculated according to the CIE L^* a^* b^* (1976) standard, using illuminant C spectral energy distribution. In this system, L^* is the color lightness (L^* = 0 for black and L^* = 100 for white), a^* is the green (–)/red (+) axis, and b^* is the blue (–)/yellow (+) axis.

3. Results and discussion

Typical X–ray diffraction patterns for the Er^{3+} doped CeO_2 nanoparticles, heat treated at 600, 900 and 1200 ºC for 4 h in air are shown in Fig. 1. All synthesized nanopowders were single–phased and exhibited the fluorite crystal structure, independent of dopant concentration in the investigated concentration range. High solubility may be attributed to nanometric nature of powders.

Besides, the calcined powders are depicted by sharper diffraction lines (Fig. 1) resulting from the increased crystallite size (D_{XRPD}), which is the consequence of increased temperature (Table 1). On the other hand, the lattice parameter (a_{XRPD}) and the microstrain (e_{XRPD}) values decreased with increasing of temperature (Table 1). The results presented in Table 1 also indicate that the lattice parameters Er^{3+} doped CeO_2 (independent of dopant concentration) were lower comparing to the lattice parameter of pure CeO_2 [35]. According to Shannon's compilation [46], the ionic radii of Ce^{4+} and Er^{3+} for the coordination number (CN) 8, are 0.970 and 1.004 Å respectively, which should result in the dilation of the lattice. However, with the increasing concentration of Er^{3+} ion the cubic lattice of ceria shrinks, which is in agreement with the theoretical results, obtained by ion–packing model [47], as well as the literature data [48, 49]. Namely, it is known that crystal lattice CeO_2 contains Ce^{4+} and Ce^{3+} ions (core–shell model) [50, 51], which in doping process may lead to the substitution of Ce^{3+} and Ce^{4+} ions with ions of Er^{3+} (confirmed by Raman spectroscopy shown below). Basically, it can be said that since the ionic radius of Er^{3+} is smaller

than the ionic radius of Ce^{3+} (1.143 Å) and larger than the ionic radius of Ce^{4+}, the result of above mentioned process is the reduction of the lattice parameter. In addition, heating at elevated temperature resulted in further reduction of the values of lattice parameters (Table 1), indicating the valence change from Ce^{3+} to Ce^{4+} due to higher thermodynamic stability of Ce^{4+} at higher temperature in air. All values of lattice parameters, crystallite size and microstrain obtained by XRPD analysis of the $Ce_{1-x}Er_xO_{2-\delta}$ nanopowders (x = 0.05–0.20) heat treated at 600, 900 and 1200 ºC for 4 h in air, are shown in Table 1.

Raman spectroscopy revealed the presence of only one phase in all the synthesized powders, which was also found by XRPD. Raman spectra of all nanometric single–phase solid solutions $Ce_{1-x}Er_xO_{2-\delta}$ (x = 0.05–0.20), calcined at 600, 900 and 1200 ºC are presented in Fig. 2. For the comparison, Raman spectra of the $Ce_{1-x}Er_xO_{2-\delta}$ (x = 0.05–0.20) at room temperature (25 ºC) were already reported in our previous work [44].The main feature of the first order Raman spectrum of pure CeO_2 is an F_{2g} mode located at 465 cm^{-1} [35]. In pure and doped CeO_2 powders obtained by SPRT method this mode is shifted to lower energies (458 cm^{-1}), with increased line width and pronounced asymmetry at low energy side [35]. Nanosize effects like phonon confinement, strain and nonstoichiometry can contribute to the observed changes in Raman peak profile [52]. After calcination at 600, 900 and 1200 ºC, this Raman mode was shifted to higher frequencies. Its line width was reduced and became more symmetrical, especially in the spectra of the samples heat treated at 1200 ºC (Fig. 2). This confirmed that thermal treatment led to grain growth and better–ordered structures.

Moreover, in the spectrum of Er^{3+} doped CeO_2 obtained before thermal treatment additional modes can be observed at around 550 and 600 cm^{-1} [44]. The Raman mode of the second order at around 600 cm^{-1} is also related to the particle size. Namely, with decreasing of particle size in undoped ceria the overall free surface of powder increases enabling in that way the easier release

of oxygen from the lattice, thus leaving the vacancy and two electrons localized on cerium atoms. This causes the lowering of cerium ion valence due to electroneutrality demands. On the other hand, the Raman mode positioned at around 550 cm^{-1} is related to oxygen vacancies formed due to the presence of dopant ions. With increasing of calcination temperature the intensity of these modes becomes weaker and at 1200 ºC completely disappears. The reason for the absence of above mentioned modes can also be valence change from Ce^{3+} to Ce^{4+} due to higher thermodynamic stability of Ce^{4+} at higher temperature in ambient atmosphere. In this way it was confirmed again that the thermally treated samples had better–ordered structure. Besides, the presence, i.e., absence of above mentioned Raman modes (Fig. 2) for all samples $Ce_{1-x}Er_xO_{2-\delta}$ (x = 0.05–0.20) confirmed the influence of concentration of Er^{3+} ions and temperature on microstructure properties, and it is in accordance with XRPD data. All these effects for all samples can be seen in Fig. 2.

The TEM images of all powders CeO_2 doped with different concentration Er^{3+} ions (x = 0.05–0.20) heat treated at 600, 900 and 1200 ºC for 4 h in air, are presented in Fig. 3. For the comparison, TEM images of the $Ce_{1-x}Er_xO_{2-\delta}$ (x = 0.05–0.20) at room temperature (25 ºC) were already reported in our previous work [44]. All images show that the crystallites tended to agglomerate and form aggregates. Such finding has also been reported in literature [27]. Namely, nanoparticles have a natural tendency to agglomerate for two main reasons. First, the agglomeration is a more stable configuration from the energetic point of view. Furthermore, nanoparticles tend to agglomerate to allow the crystallite growth. It is noteworthy that the mean crystallite size, calculated from TEM images (Fig. 3) shows tended decrease with increasing of concentration of the Er^{3+} ions for each temperature (Table 1). Generally, the mean crystallite size for the 5 % Er^{3+} doped sample was larger than the one for 20 % Er^{3+} doped sample for each temperature. On the other hand, with increasing of temperature, the values of mean crystallite

size shows tended increase. Thus, the obtained results indicate that the mean crystallite sizes measured from the TEM images differs at most by 1 nm from those obtained by XRPD, confirming its consistence with the results obtained by XRPD.

Additional information about the morphology and composition of the $Ce_{0.95}Er_{0.05}O_{2-\delta}$ and $Ce_{0.80}Er_{0.20}O_{2-\delta}$ nanopowders heat treated at 1200 ºC for 4h in air, as the representative ones, were obtained by SEM observation (Figs. 4a and 4b) and EDS analysis (Figs. 4a and 4b–inset). As shown in the SEM images (Figs. 4a and 4b), these two samples exhibited homogeneous structure and no obvious difference between the two samples in the morphology was found, implying that the samples have good thermal stability. The average grain size was smaller than 40 nm, which is again in good agreement with particle size obtained by XRPD analysis. The corresponding EDS images (Figs. 4a and 4b–inset) and mean value of the Ce/Er chemical ratio confirmed that the Er^{3+} ions in the concentrations of 5 (Ce/Er = 95.18/4.82) and 20 % (Ce/Er = 81.45/18.55) successfully doped into the host matrix.

Fig. 5 shows the FTIR spectra of sample $Ce_{0.90}Er_{0.10}O_{2-\delta}$, as the representative of all samples, before and after heat treatment at 900 ºC for 4 h in the ambient atmosphere. Both spectra present a large absorption band located at around 500 cm^{-1}, which can be attributed to the Ce–O stretching vibration [22, 53, 54], and corresponds to the F1u IR active mode of the CeO_2 fluorite structure. In addition, the bands located at around 725, 840, and 1063 cm^{-1} can been attributed to the CO_2 asymmetric stretching vibration, CO_3^{2-} bending vibration, and C–O stretching vibration, respectively [55]. These bands are linked to the presence of atmospheric CO_2 adsorbed on the cations [27] and the formation of "carbonate–like" species on the particle surfaces [53] as a consequence of the reaction of atmospheric CO_2 with water and sodium hydroxide during the synthesis. The bands located at around 1340 and 1500 cm^{-1} could be attributed to carbonate species vibrations [53, 55] or to nitrate spices. However, these clearly attenuated bands after heat

treatment indicating that the carbonate species were decomposed by heat treatment. The band located at around 1640 cm^{-1} is attributed to the H–O–H bending vibration [27], and indicates the presence of water. Both spectra contain a large band with the maximum located at around 3400 cm^{-1}, which can be attributed to the O–H stretching vibration [22]. It confirms the presence of moisture and structural water in the sample before its exposure to elevated temperature. Since the band is attenuated in the spectrum collected after heat treatment at 900 ºC for 4 h in air, it can be concluded that some moisture was absorbed after calcination.

The influence of temperature on the optical properties of the ceramic samples $Ce_{1-x}Er_xO_{2-\delta}$ (x = 0.05–0.20), obtained both at room temperature (25 ºC) and heat treated at 600, 900 and 1200 ºC for 4 h in air, was investigated (Fig. 6). Particularly, the absorbance and the band gap energy were examined by UV–VIS diffuse reflectance spectroscopy. Diffuse reflectance spectra of the $Ce_{1-x}Er_xO_{2-\delta}$ samples, are separately presented for each mole fraction x in Fig. 6.

As can be seen in Figs. 6a, 6c, 6e and 6g, the incorporation of Er^{3+} in CeO_2 lattice results in the reflectance minimum at around 360–390 nm (which means that complementary absorption band is in the same region) while the reflectance maximum is centered in the blue region (460–480 nm). Absorption edge around 380 nm is ascribed to the charge transfer of $O_{2p} \rightarrow Ce_{4f}$ [56]. It is noticeable that increasing temperature results in increasing absorption, especially for the samples treated at 1200 ºC (Figs. 6a, 6c, 6e and 6g). On the reflectance plateau the intensive absorption peaks at 490 nm, 520 nm, 546 nm, 652 nm and 677 nm can be found. The intensity of mentioned peaks increases correspondingly with the change of Er^{3+} mole fraction from 0.05 to 0.2. Due to these findings, the intensive absorption peaks at 520 nm and 652 nm are assigned to $^4I_{15/2} \rightarrow F_{11/2}$ and $^4I_{15/2} \rightarrow F_{9/2}$ of Er^{3+} ions, respectively. Peaks around 550 nm and 670 nm are assigned to the transition of $^4S_{3/2} \rightarrow {}^4I_{15/2}$ and $^4F_{9/2} \rightarrow {}^4I_{15/2}$ of Er^{3+} ions [56].

The changes of pick intensity (ΔR) at 520 nm (the intensive absorption peak on the reflectance plateau) with Er^{3+} mole fraction *x* at room temperature (25 ºC) and heat treated at temperatures 600, 900 and 1200 ºC are represented on Fig. 7. The change of peak intensity (ΔR_{520nm}) is defined as the difference between plateau reflectance ($R_{plateau}$) and reflectance at 520 nm (R_{520nm}), for each reflectance spectrum: $\Delta R_{520nm}=R_{plateau}-R_{520nm}$.

The peak intensity at 520 nm increases with the increasing content of Er^{3+} ions in $Ce_{1-x}Er_xO_{2-\delta}$, which is not surprising since the peak originates from the absorption of Er^{3+} ions. As shown in Figs. 6a, 6c, 6e and 6g, the intensity of absorption peak at 520 nm should reach saturation for the samples with erbium mole fraction greater than 0.15. It can be concluded that with increasing of erbium mole fraction above 0.15, a stronger interaction (which resulted in the saturation of absorption) between Er^{3+}–Er^{3+} dopants occurred in the $Ce_{1-x}Er_xO_{2-\delta}$ samples. Besides that, the heating at the elevated temperature resulted in a better absorption of Er^{3+} ions. As it can be seen in Fig. 7., the peak intensity rise is larger for the samples treated at 900 and 1200 ºC than for samples annealed at 600 ºC. This might be attributed to the difference in crystallite size, which is three times smaller for the ceramic samples obtained at 600 ºC in comparison to the samples heat treated at 1200 ºC (Table 1).

In addition, from presented reflectance curves (Figs. 6a, 6c, 6e and 6g), the direct band gap energies (E_g) of the $Ce_{1-x}Er_xO_{2-\delta}$ (x = 0.05–0.20) nanopowders at 25 ºC and heat treated at 600, 900 and 1200 ºC for 4 h in air were calculated from the Tauc plot [57], using the Kubelka–Munk function [58]. The diffuse reflectance R is related to the Kubelka–Munk function F(R) by Eq. (3):

$$F(R)=\frac{(1-R)^2}{2R} \tag{3}$$

where R is the reflectance. After calculating the F(R) value from the Eq. (3), $[F(R)\times E]^2$ was plotted versus energy E in electron volts. The direct band gap energies (E_g) of the $Ce_{1-x}Er_xO_{2-\delta}$ nanopowders (x = 0.05–0.20) at room temperature and treated at different temperatures, were determined by the extrapolation of the linear part of the curves to $[F(R)\times E]^2 = 0$, and presented in Table 2.

Thus, from Figs. 6a, 6c, 6e and 6g was evident that $Ce_{1-x}Er_xO_{2-\delta}$ (x = 0.05–0.20) samples obtained at 25 ºC and heat treated at 600, 900 and 1200 ºC for 4 h in air, have different reflectance spectrum with dissimilar reflectance plateaus due to absorption. The reflectance of the all above mentioned samples Er^{3+} doped CeO_2 also, at mentioned temperatures, exhibits different slopes with wavelength below 400 nm (Figs. 6a, 6c, 6e and 6g). It can be said that these slopes are in relation with the temperature. For example, using Kubelka–Munk method the calculated band gap energies (and consequently absorption edge) for $Ce_{0.95}Er_{0.05}O_{2-\delta}$ samples at different temperature is within the limits from 3.25 eV at 25 ºC to 3.08 eV at 1200 ºC (Table 2.). These energy values correspond to 381 nm and 402 nm, respectively. Therefore, the increasing of temperature results in slightly shift (about 20 nm) of reflectance curve towards longer wavelengths and this small shift can be observed on reflectance spectrum below 400 nm in Fig. 6a. Generally, the increase of the mole fraction of Er^{3+} ions and temperature decreased the band gap, which is obvious when band gap values for x=0.05 and x=0.2 at different temperatures are compared (Table 2). It can be said that the introduction of Er^{3+} into ceria (CeO_2) lattice resulted in the thermodynamic stability of the lattice, which reduced the band gap energy. The highest value of band gap was detected for the sample that was not submitted to the thermal treatment (Table 2). This is in a good agreement with literature data [59]. It is interesting that the sample annealed at 600 ºC exhibited a small reduction of band gap, while the greatest observed band gap

energy drop was between the samples thermally treated at 900 and 1200 ºC. Therefore, it is obvious that the increasing of temperature and mole fraction of Er^{3+} ions increased the absorption and slightly shifted the absorption edge towards lower energies (Table 2). So, increase of temperature, as well as concentration of Er^{3+} leads to a decreased the band gap width.

In accordance with registered changes of band gap width and color characteristics of the $Ce_{1-x}Er_xO_{2-\delta}$ (x = 0.05–0.20) samples (Fig. 6), the values of chromatic coordinates of the pigments together with the band gap calculated values are presented in Table 2. Chromatic diagrams of CeO_2 nanopowders doped with different concentration of Er^{3+} ($Ce_{1-x}Er_xO_{2-\delta}$, x = 0.05–0.20) obtained at room temperature (25 ºC), and heat treated at 600, 900 and 1200 ºC for 4 h in air are illustrated in Figs. 6b, 6d, 6f and 6h [60]. Generally, for prepared samples $Ce_{1-x}Er_xO_{2-\delta}$ (x = 0.05–0.20) the progressive decrease (from 86.036 to 61.122) of luminosity (L^*), i.e. further increase in the color intensity with increase of concentration Er^{3+} ions and temperature, may support the thesis about the incorporation of Er^{3+} ions in the lattice of CeO_2. With increasing of concentration of Er^{3+} ions and temperature of heat treatments, the values of L^* decrease and the color shifted from white–pink toward light–pink hue (increasing a^*). The highest pink component (the highest value of coordinates a^*) is reached in the pigment corresponding to the highest concentration of Er^{3+} ions ($Ce_{0.80}Er_{0.20}O_{2-\delta}$) heat treated at the highest temperature (1200 ºC). Thus, as it could be seen (Figs. 6b, 6d, 6f and 6h; insets–visual appearance at 900 ºC), the color of pigments depend on the composition and temperature, and with increasing of Er^{3+} ions content varies from white–pink to light–pink hue.

4. Conclusion

New inorganic pigments $Ce_{1-x}Er_xO_{2-\delta}$ (x = 0.05–0.20) as solid solutions were prepared by the self–propagating room temperature method (SPRT), which is easy to handle and low cost. The

ceria powders containing all investigated Er^{3+} dopant concentrations at 25 ºC and calcined at all investigated temperatures (600, 900 and 1200 ºC), were solid solutions with fluorite structure. All the obtained $Ce_{1-x}Er_xO_{2-\delta}$ pigments were found to be thermally stable and with particle sizes within the nanometric range. Their color depended on the composition and temperature, and with increasing Er^{3+} content varied from white–pink to light–pink hue. Increasing calcinations temperature resulted in the increase of crystallite size, which led to increasing absorption and shifting of the edge of absorption of visible light towards lower energies. As a consequence, dominant wavelength of the color shifted towards pink hue, becoming more saturated with temperature. Therefore, the obtained pigments might find potential alternative to the classical toxic pink inorganic pigments for various applications such as paints, coatings, ceramics, cosmetics, plastics and glass enamels.

Acknowledgement

This work was supported by the Serbian Ministry of Education, Science, and Technological Development through the projects III 45012, III 45001, III 45007 and 172015. The authors are also grateful to A.von Humboldt foundation for supporting this work.

References

[1] Khichar N, Bishnoi S, Chawla S, Introducing dual excitation and tunable dual emission in ZnO through selective lanthanide (Er^{3+}/Ho^{3+}) doping, RSC Adv 2014; 4: 18811–18817.

[2] Song L, Liu X, Zhen Z, Chen C, Zhang D, Solution–processable erbium–ytterbium complex for potential planar optical amplifier application, J Mater Chem 2007; 17: 4586–4590.

[3] Li H, Jia Y, Sun W, Zhao R, Fu J, Jiang J, Zhang S, Pang R, Li C, Novel energy transfer mechanism in single–phased color–tunable $Sr_2CeO_4:Eu^{3+}$ phosphors for WLEDs, Optical Materials 2014; 36: 1883–1889.

[4] Lemdek EM, Benkhouja K, Touhtouh S, Sbiaai K, Arbaoui A, Bakasse M, Hajjaji A, Boughaleb Y, Saez–Puche R, Influence of Ca^{2+} doped on structural and optical properties of RPO_4 (R = Ce^{3+}, Nd^{3+} and Pr^{3+}) compounds, Optical Materials 2013; 36: 86–90.

[5] Gheno G, Bortoluzzi M, Ganzerla R, Enrichi F, Inorganic pigments doped with tris(pyrazol–1–yl)borate lanthanide complexes: A photoluminescence study, J Luminesc 2014; 145: 963–969.

[6] Prabhakar Rao P, Reddy MLP, Synthesis and characterisation of $(BiRE)_2O_3$ (RE: Y, Ce) pigments, Dyes Pigment 2004; 63: 169–174.

[7] Jansen M, Letschert HP, Inorganic yellow–red pigments without toxic metals, Nature 2000; 404: 980–982.

[8] Prabhakar Rao P, Reddy MLP, $(TiO_2)_1(CeO_2)_{1-x}(RE_2O_3)_x$ – novel environmental secure pigments, Dyes Pigment 2007; 73: 292–297.

[9] Furukawa S, Masui T, Imanaka N, New environment–friendly yellow pigments based on CeO_2–ZrO_2 solid solutions, J Alloys Compd 2008; 451: 640–643.

[10] Olazcuaga R, Polles GL, Kira AE, Flem GL, Maestro P, Optical properties of $Ce_{1-x}Pr_xO_2$ powders and their applications to the coloring of ceramics, J Solid State Chem 1987; 71: 570–573.

[11] Maso N, Beltran H, Munoz R, Julian B, Carda JB, Escribano P, Cordoncillo E, Optimization of Praseodymium–Doped Cerium Pigment Synthesis Temperature, J Am Ceram Soc 2003; 86: 425–430.

[12] Šulcová P, Trojan M, The synthesis of the $Ce_{0.95-y}Pr_{0.05}La_yO_{2-y/2}$ pigments, Dyes Pigment 2000; 44: 165–168.

[13] Šulcová P, Trojan M, The synthesis and analysis of $Ce_{0.95-y}Pr_{0.05}Sm_yO_{2-y/2}$ pigments, Dyes Pigment 2003; 58: 59–63.

[14] Tnunekawa S, Fukuda T, Kasuya A, Blue shift in ultraviolet absorption spectra of monodisperse CeO_{2-x} nanoparticles, J Appl Phys 2000; 87: 1318–1321.

[15] Tnunekawa S, Wang JT, Kawazoe Y, Kasuya A, Blueshifts in the ultraviolet absorption spectra of cerium oxide nanocrystallites, J Appl Phys 2003; 94: 3654–3656.

[16] Eppler RA, in: Hench LL, Dove DB(Eds.), Physics of Electronic Materials, Part B, Marcel Dekker, New York; 1972, p. 1021.

[17] Aruna ST, Ghosk S, Patil KC, Combustion synthesis and properties of $Ce_{1-x}Pr_xO_{2-\delta}$ red ceramic pigments, Int J Inorg Mater 2001; 3: 387–392.

[18] Šulcová P, Trojan M, Study of $Ce_{1-x}Pr_xO_2$ pigments, Thermochim Acta 2002; 395: 251–255.

[19] Santos SF, De Andrade MC, Sampaio J A, da Luz AB, Ogasawara T, Synthesis of ceria–praseodymia pigments by citrate–gel method for dental restorations, Dyes Pigment 2007; 75: 574–579.

[20] Masui T, Furukawa S, Imanaka N, Synthesis and Characterization of CeO_2–ZrO_2–Bi_2O_3 Solid Solutions for Environment–friendly Yellow Pigments, Chemistry Letters 2006; 35: 1032–1033.

[21] Adachi G–y, Imanaka N, The Binary Rare Earth Oxides, Chemical Reviews 1998; 98: 1479–1514.

[22] Wang T, Sun DC, Preparation and characterization of nanometer–scale powders ceria by electrochemical deposition method, Mater Res Bull 2008; 43: 1754–1760.

[23] Tock AIY, Boey FYC, Dong Z, Sun XL, Hydrothermal synthesis of CeO_2 nanoparticles, J Mater Process Technol 2007; 190: 217–222.

[24] Lu X, Li X, Chen F, Ni C, Chen Z, Hydrothermal synthesis of prism–like mesocrystal CeO_2, J Alloys Compd 2009; 476: 958–962.

[25] Zhou F, Ni X, Zhang Y, Zheng H, Size–controlled synthesis and electrochemical characterization of spherical CeO_2 crystallites, J Colloid Interface Sci 2007; 307: 135–138.

[26] Ho C, Yu JC, Kwong T, Mak AC, Lai S, Morphology–controllable synthesis of mesoporous CeO_2 nano– and microstructure, Chem Mater 2005; 17: 4514–4522.

[27] Phoka S, Laokul P, Swatsitang E, Promarack V, Synthesis, structural and optical properties of CeO_2 nanoparticles synthesized by a simple polyvinyl pyrrolidone (PVP) solution route, Mater Chem Phys 2009; 115: 423–428.

[28] Skofic IK, Sturm S, Ceh M, Bukovec N, CeO_2 thin films obtained by sol–gel deposition and annealed in air or argon, Thin Solid Films 2002; 422: 170–175.

[29] Liu ZL, Yue HM, Wang Y, Yao KL, Liu Q, The VCNR properties of nano–structured ceria thin films, Solid State Commun 2002; 124: 171–176.

[30] Yabe S, Yamashita M, Momose S, Tahira K, Yoshida S, Li R, Yin S, Sato T, Synthesis and UV–shielding properties of metal oxide doped ceria via soft solution chemical processes, Int J Inorg Mater 2001; 3: 1003–1008.

[31] Li R, Yabe S, Yamashita M, Momose S, Yoshida S, Yin S, Sato T, Synthesis and UV–shielding properties of ZnO– and CaO–doped CeO_2 via soft solution chemical process, Solid State Ionics 2002; 151: 235–241.

[32] Yabe S, Tsugio S, Cerium oxide for sunscreen cosmetics, J Solid State Chem 2002; 171: 7–11.

[33] Yue L, Zhang XM, Structural characterization and photocatalytic behaviors of doped CeO_2 nanoparticles, J Alloy Compd 2008; 475: 702–705.

[34] Godinho MJ, Goncalvez RF, Santos LPS, Varela JA, Longo E, Leite ER, Room temperature co–precipitation of nanocrystalline CeO_2 and $Ce_{0.8}Gd_{0.2}O_{1.9-\delta}$ powder, Mater Lett 2007; 61: 1904–1907.

[35] Stojmenović M, Bošković S, Zec S, Babić B, Matović B, Bučevac D, Dohčević–Mitrović Z, Aldinger F, Characterization of nanometric multidoped ceria powders, J Alloy Compd 2010; 507: 279–285.

[36] West AR, Solid State Chemistry and its Applications. Wiley, New York: 1991, p. 36–64.

[37] Dann SE, Reactions and Characterization of Solids. Wiley, New York: 2000, p. 141–148.

[38] Wang S, Maeda K, Awano M, Direct Formation of Crystalline Gadolinium–Doped Ceria Powder via Polymerized Precursor Solution, J Am Ceram Soc 2002; 85: 1750–1752.

[39] Zhong SW, Zhang Q, Han DQ, Kuang JZ, Preparation of Color Pearlescent Pigment Using Rare–Earth Oxide and Titanium Oxide to Coat Mica, Key Engineering Materials 2005; 280–283: 903–906.

[40] Michae CP, Yuen HB, Sabnis VA, Johnson TJ, Sewell R, Smith R, Jamora A, Clark A, Semans S, Atanackovic PB, Painter O, Growth, processing, and optical properties of epitaxial Er_2O_3 on silicon, Optics express 2008; 16: 19649–19666.

[41] Kaewwiset W, Thamaphat K, Kaewkhao J, Limsuwan P, Er^{3+}–doped soda–lime silicate glass: artificial pink gemstone, American Journal of Applied Sciences 2012; 9: 1769–1775.

[42] Jha AR, Rare Earth Materials: Properties and Applications, CRC Press Taylor & Francis Group; 2014.

[43] Truffault L, Yao QW, Wexler D, Nevirkovets IP, Konstantinov K, Devers T, Nightingale S., Synthesis and characterization of Fe doped CeO_2 nanoparticles for pigmented ultraviolet filter applications, J Nanosci Nanotechnol 2011; 11: 4019–4028.

[44] Stojmenović M, Bošković S, Žunić M, Babić B, Matović B, Bajuk–Bogdanović D, Menus S, Studies on structural, morphological and electrical properties of $Ce_{1-x}Er_xO_{2-\delta}$ (x = 0.05 - 0.20) as solid electrolyte for IT – SOFC, Mat Chem Phys, 153 (2015) 422–431.

[45] Suryanarayana C, Grant Norton M, X–ray Diffraction: A Practical Approach, Springer, New York; 1998.

[46] Shannon RD, Revised effective ionic radii and systematic studies of interatomic distances in halides and chalcogenides, Acta Crystallogr 1976; A32: 751–767.

[47] Hong SJ, Virkar AV, Lattice parameters and densities of rare earth oxide doped ceria electrolytes, J Am Ceram Soc 1995; 78: 433–439.

[48]. Pikalova EY, Murashkina AA, Maragou VI, Demin AK, Strekalovsky VN, Tsiakaras PE, CeO_2 based materials doped with lanthanides for applications in intermediate temperature electrochemical devices, Int J Hydrogen Energy 2011; 36: 6175–6183.

[49] Mandal BP, Roy M, Grover V, Tyagi AK, X–ray diffraction, μ–Raman spectroscopic studies on CeO_2–RE_2O_3 (RE=Ho, Er) systems: Observation of parasitic phases, J Appl Phys 2008; 103: 0335061–0335067.

[50] Wu L, Wiesmann HJ, Moodenbaugh AR, Klie RF, Zhu Y, Welch DO, Suenaga M, Oxidation state and lattice expansion of CeO_{2-x} nanoparticles as a function of particle size, Phys Rev B 2004; 69: 125415–125416.

[51] Tsunekawa S, Ito S, Kawazoe Y, Surface structures of cerium oxide nanocrystalline particles from the size dependence of the lattice parameters, Appl Phys Lett 2004; 85: 3845–3847.

[52] Spanier E, Robinson RD, Zhang F, Chan SW, Herman IP, Size–dependent properties of CeO_{2-y} nanoparticles as studied by Raman scattering, Phys Rev B 2001; 64: 245407–245407.

[53] Andreescu D, Matijevic E, Goia DV, Formation of uniform colloidal ceria in polyol, Colloids Surf A 2006; 291: 93–100.

[54] Liu J, Zhao Z, Wang J, Xu C, Duan A, Jiang G, Yang Q, The highly active catalysts of nanometric CeO_2–supported cobalt oxides for soot combustion, Appl Catal B 2008; 84: 185–195.

[55] Wang S, Gu F, Li C, Cao H, Shape–controlled synthesis of $CeOHCO_3$ and CeO_2 microstructures, J Cryst Growth 2007; 307: 386–394.

[56] Xijuan Y, Pingbo X, Qingde S, Size–dependent optical properties of nanocrystalline CeO_2:Er obtained by combustion synthesis, Phys Chem Chem Phys 2001; 3: 5266–5269.

[57] Tauc J, Grigorovici R, Vancu A, Optical Properties and Electronic Structure of Amorphous Germanium, Physica Status Solidi (b) 1966; 15: 627–637.

[58] Cavalcante LS, Longo VM, Sczancoski JC, Almeida MAP, Batista AA, Varela JA, Orlandi MO, Longo E, Siu Li M, Electronic structure, growth mechanism and photoluminescence of $CaWO_4$ crystals, Cryst Eng Comm 2012; 14: 853–868.

[59] Masui T, Fujiwara K, Machida K, Adachi G, Sakata T, Mori H, Characterization of cerium (IV) oxide ultrafine particles prepared using reversed micelles, Chem Mater 1997; 9: 2197–2204.

[60] Commission internationale de l'Eclairage proceedings 1931. Cambridge University Press, Cambridge, 1932.

Figure captions:

Fig. 1. X–ray diffraction patterns of: a) $Ce_{0.95}Er_{0.05}O_{2-\delta}$, b) $Ce_{0.90}Er_{0.10}O_{2-\delta}$, c) $Ce_{0.85}Er_{0.15}O_{2-\delta}$ and d) $Ce_{0.80}Er_{0.20}O_{2-\delta}$ nanopowders, heat treated at 600, 900 and 1200 ºC for 4 h in air.

Fig. 2. Raman spectra of: a) $Ce_{0.95}Er_{0.05}O_{2-\delta}$, b) $Ce_{0.90}Er_{0.10}O_{2-\delta}$, c) $Ce_{0.85}Er_{0.15}O_{2-\delta}$ and d) $Ce_{0.80}Er_{0.20}O_{2-\delta}$ nanopowders, heat treated at 600, 900 and 1200 ºC for 4 h in air.

Fig. 3. TEM images of $Ce_{1-x}Er_xO_{2-\delta}$ (x = 0.05–0.20) nanopowders heat treated at: a) 600 ºC, b) 900 ºC and c) 1200 ºC, for 4 h in air.

Fig. 4. SEM images of: a) $Ce_{0.95}Er_{0.05}O_{2-\delta}$ and b) $Ce_{0.80}Er_{0.20}O_{2-\delta}$ nanopowders, heat treated at 1200 ºC for 4 h in air, with corresponding EDS spectra.

Fig. 5. FTIR spectra of the $Ce_{0.90}Er_{0.10}O_{2-\delta}$ nanopowders: a) at room temperature (25 ºC) and b) heat treated at 900 ºC for 4 h in air.

Fig. 6. The reflectance spectra and chromatic diagrams of the $Ce_{1-x}Er_xO_{2-\delta}$ nanopowders (x = 0.05–0.20) obtained without thermal treatment (25 ºC) and heat treated at 600, 900 and 1200 ºC for 4 h in air (insets–visual appearance at 900 ºC).

Fig. 7. The peak intensity changes at 520 nm of the $Ce_{1-x}Er_xO_{2-\delta}$ nanopowders (x = 0.05–0.20) obtained without thermal treatment (25 ºC) and heat treated at 600, 900 and 1200 ºC for 4h in air.

Tables:

Table 1

Lattice parameters (a_{XRPD}), crystallite size (D_{XRPD}) and microstrain (e_{XRPD}) obtained by XRPD analysis, and particle size obtained by TEM method of the $Ce_{1-x}Er_xO_{2-\delta}$ nanopowders (x = 0.05–0.20) heat treated at 600, 900 and 1200 ºC for 4 h in air.

Composition	$a_{XRPD.}$ **(Å)**	D_{XRPD} **(nm)**	e_{XRPD} **(%)**	**Particle size (TEM) /nm**
600 ºC				
1. $Ce_{0.95}Er_{0.05}O_{2-\delta}$	5.3895	12.92	0.36	12.23
2. $Ce_{0.90}Er_{0.10}O_{2-\delta}$	5.3882	11.17	0.29	11.02
3. $Ce_{0.85}Er_{0.15}O_{2-\delta}$	5.3871	11.14	0.27	10.98
4. $Ce_{0.80}Er_{0.20}O_{2-\delta}$	5.3844	10.46	0.23	10.22
900 ºC				
1. $Ce_{0.95}Er_{0.05}O_{2-\delta}$	5.3799	32.44	0.10	31.87
2. $Ce_{0.90}Er_{0.10}O_{2-\delta}$	5.3748	27.33	0.09	26.66
3. $Ce_{0.85}Er_{0.15}O_{2-\delta}$	5.3726	26.23	0.09	26.12
4. $Ce_{0.80}Er_{0.20}O_{2-\delta}$	5.3715	23.70	0.08	23.24
1200 ºC				
1. $Ce_{0.95}Er_{0.05}O_{2-\delta}$	5.3751	38.83	0.06	38.07
2. $Ce_{0.90}Er_{0.10}O_{2-\delta}$	5.3745	37.62	0.03	37.15
3. $Ce_{0.85}Er_{0.15}O_{2-\delta}$	5.3708	36.52	0.02	36.01
4. $Ce_{0.80}Er_{0.20}O_{2-\delta}$	5.3696	36.09	0.02	35.78

Table 2

Calculated band gap energy (E_g) and color coordinates (L^* a^* b^*) for the $Ce_{1-x}Er_xO_{2-\delta}$ (x = 0.05–0.20) nanopowders at 25 ºC and heat treated at 600, 900 and 1200 ºC for 4 h in air.

Composition	**Band gap**	**Color measurement**		
	E_g **(eV)**	L^*	a^*	b^*
25 ºC				
1. $Ce_{0.95}Er_{0.05}O_{2-\delta}$	3.25	78.880	-1.560	10.683
2. $Ce_{0.90}Er_{0.10}O_{2-\delta}$	3.22	84.646	1.189	23.033
3. $Ce_{0.85}Er_{0.15}O_{2-\delta}$	3.20	86.036	-10.048	16.143
4. $Ce_{0.80}Er_{0.20}O_{2-\delta}$	3.16	79.290	1.843	24.578
600 ºC				
1. $Ce_{0.95}Er_{0.05}O_{2-\delta}$	3.21	78.129	-1.253	9.042
2. $Ce_{0.90}Er_{0.10}O_{2-\delta}$	3.19	75.017	1.673	20.578
3. $Ce_{0.85}Er_{0.15}O_{2-\delta}$	3.18	75.742	2.425	20.006
4. $Ce_{0.80}Er_{0.20}O_{2-\delta}$	3.13	73.364	3.355	18.858
900 ºC				
1. $Ce_{0.95}Er_{0.05}O_{2-\delta}$	3.18	75.110	1.566	2.303
2. $Ce_{0.90}Er_{0.10}O_{2-\delta}$	3.17	75.251	3.903	16.199
3. $Ce_{0.85}Er_{0.15}O_{2-\delta}$	3.11	74.785	4.994	14.355
4. $Ce_{0.80}Er_{0.20}O_{2-\delta}$	3.05	70.486	5.243	13.663
1200 ºC				
1. $Ce_{0.95}Er_{0.05}O_{2-\delta}$	3.08	62.650	1.273	2.936
2. $Ce_{0.90}Er_{0.10}O_{2-\delta}$	3.05	62.688	4.274	15.405
3. $Ce_{0.85}Er_{0.15}O_{2-\delta}$	3.01	61.122	2.060	12.424
4. $Ce_{0.80}Er_{0.20}O_{2-\delta}$	2.96	61.515	6.139	13.367

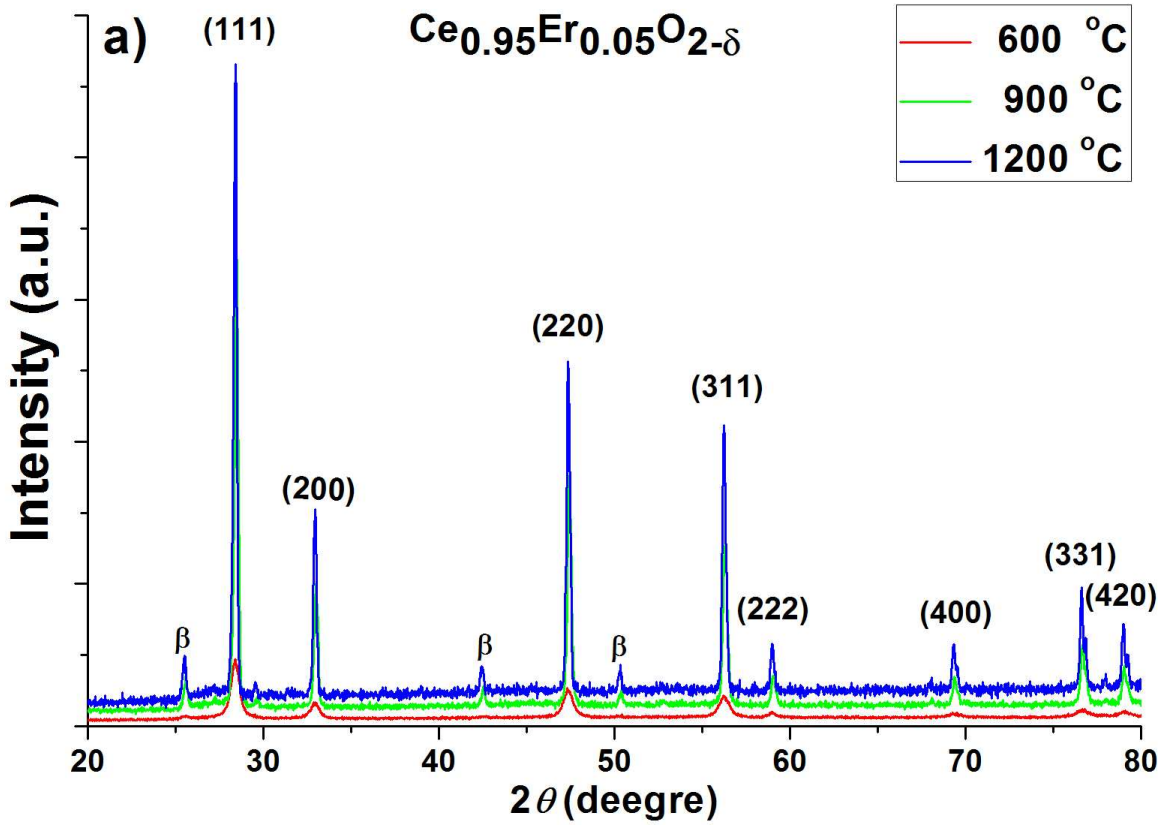

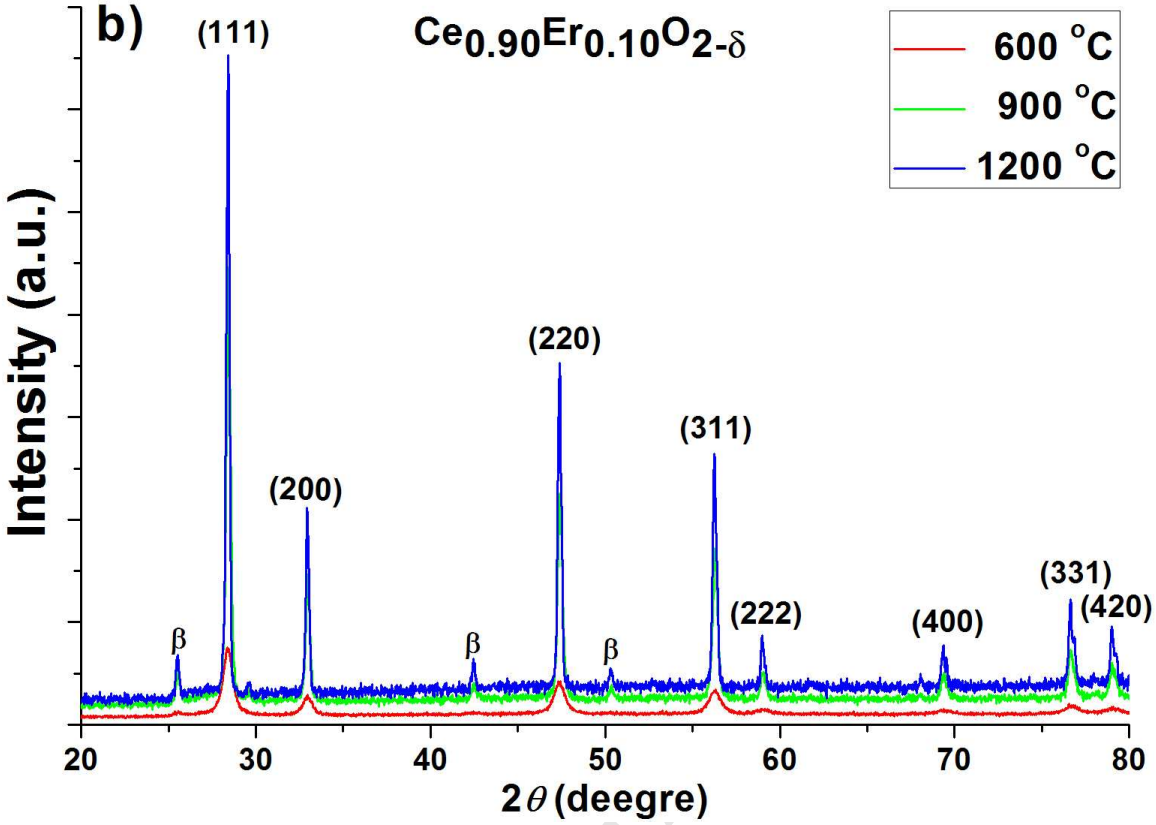

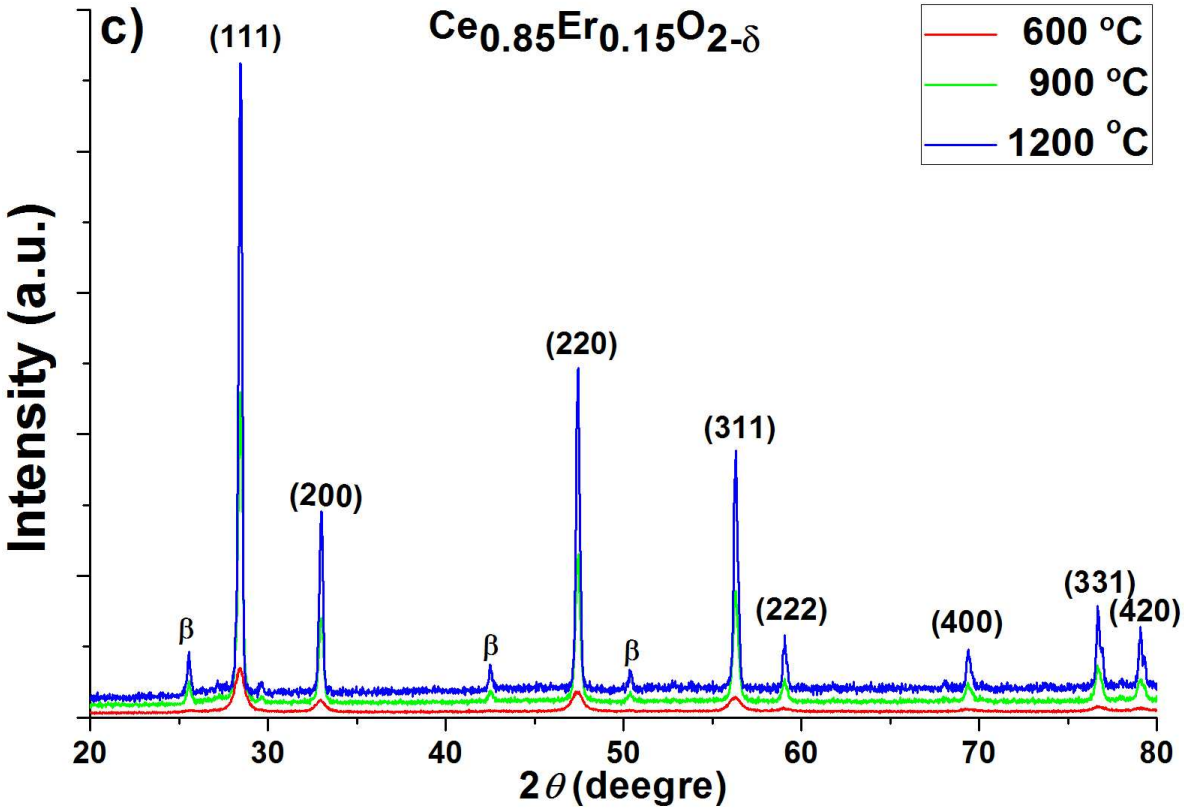

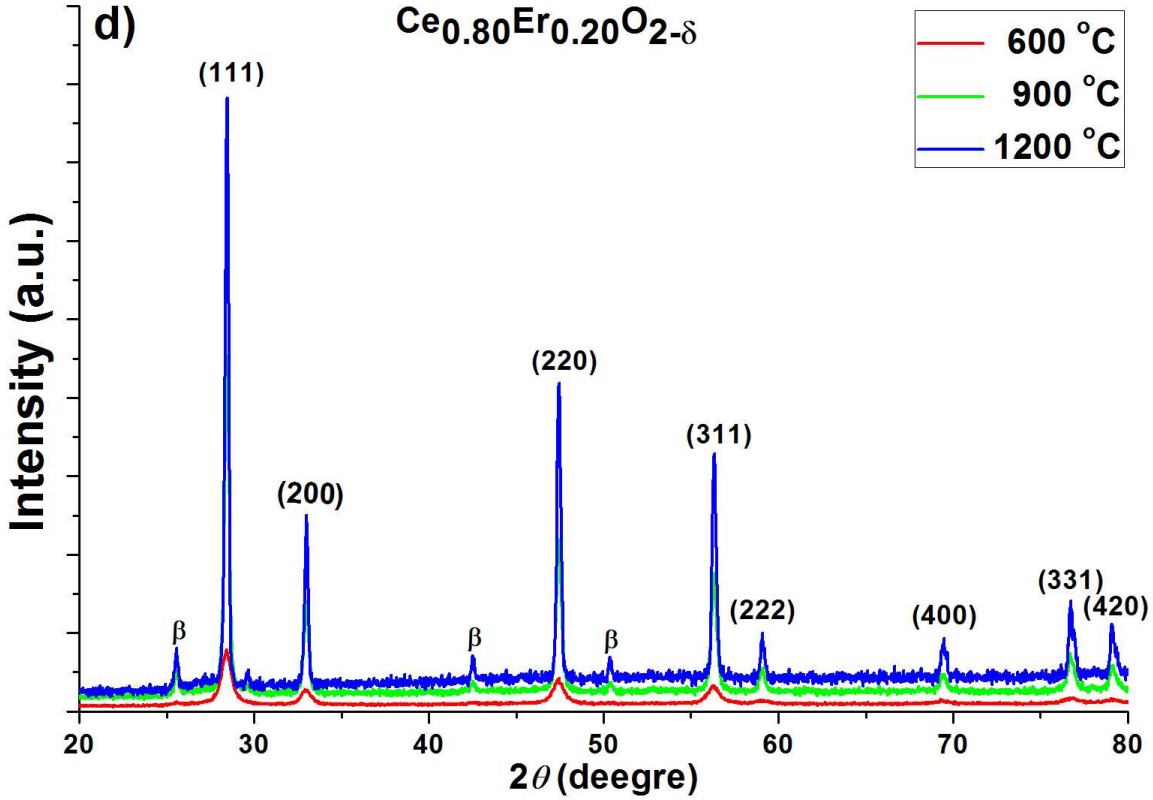

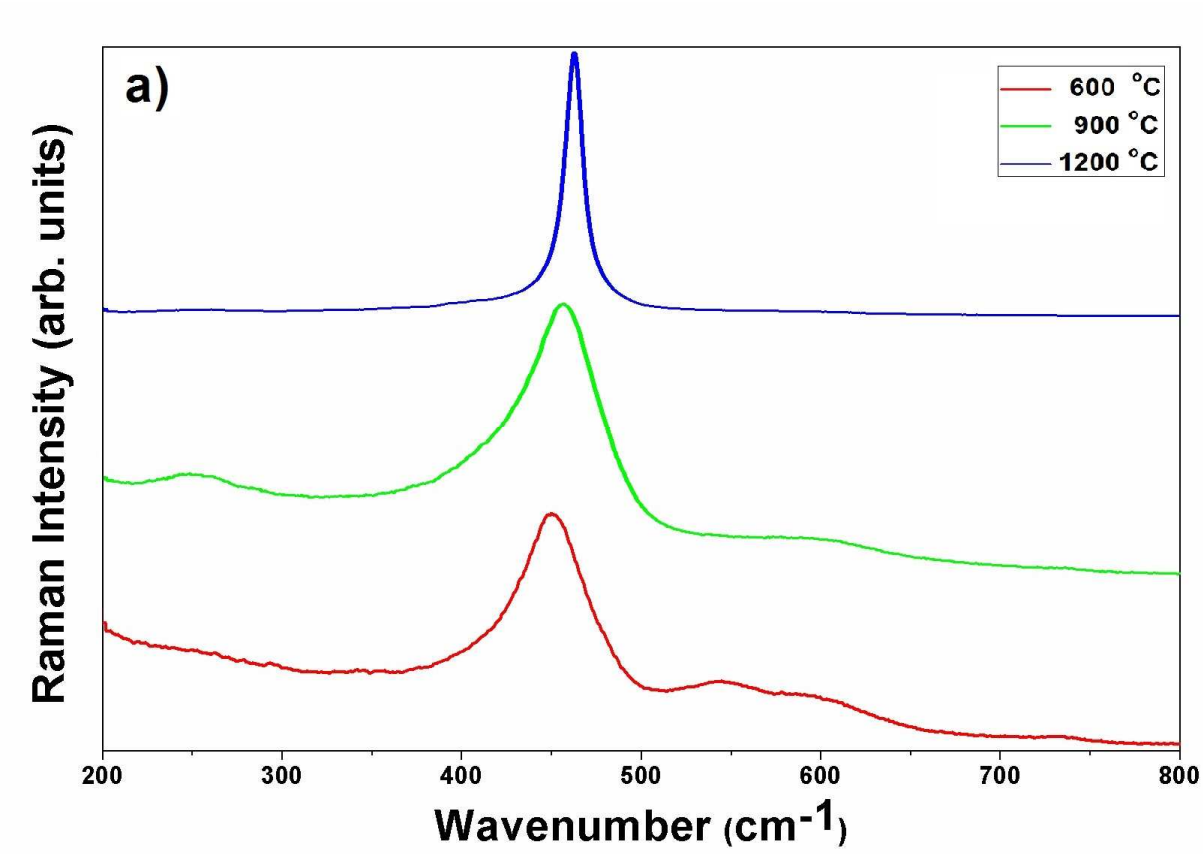

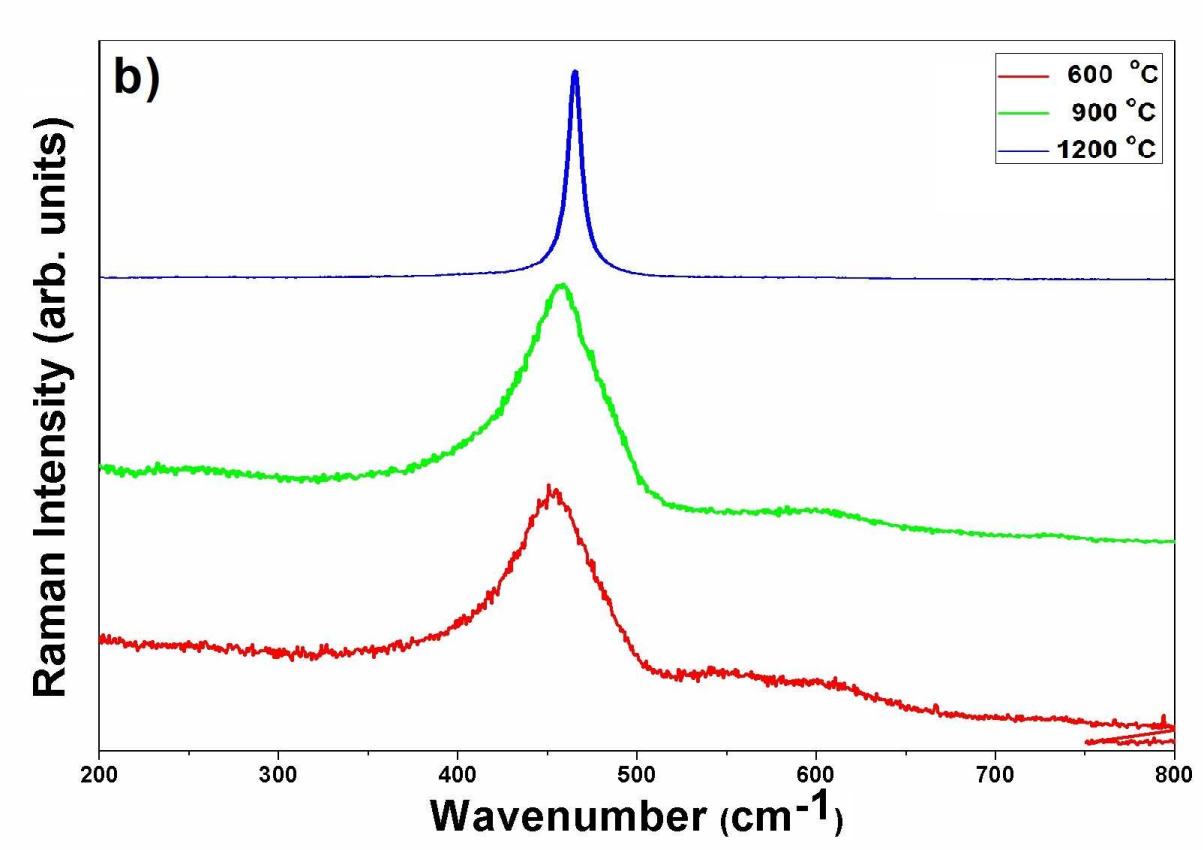

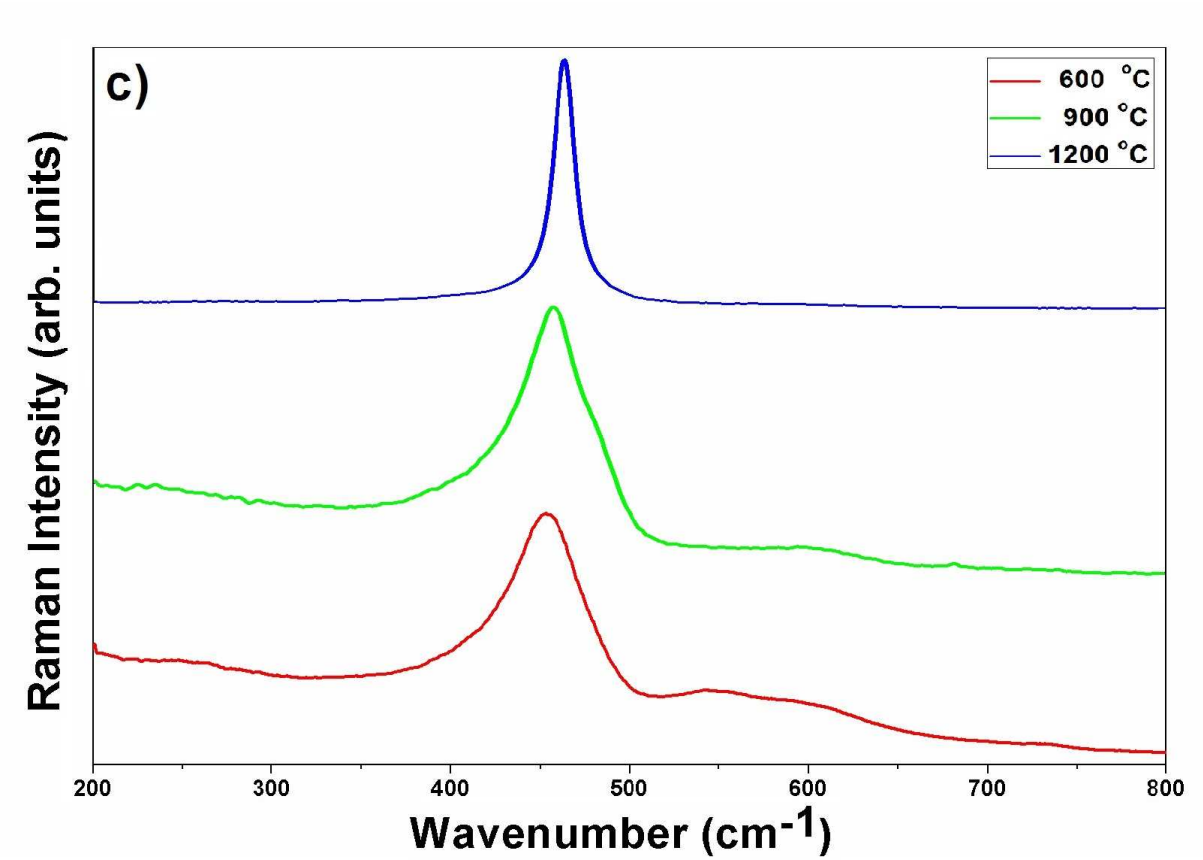

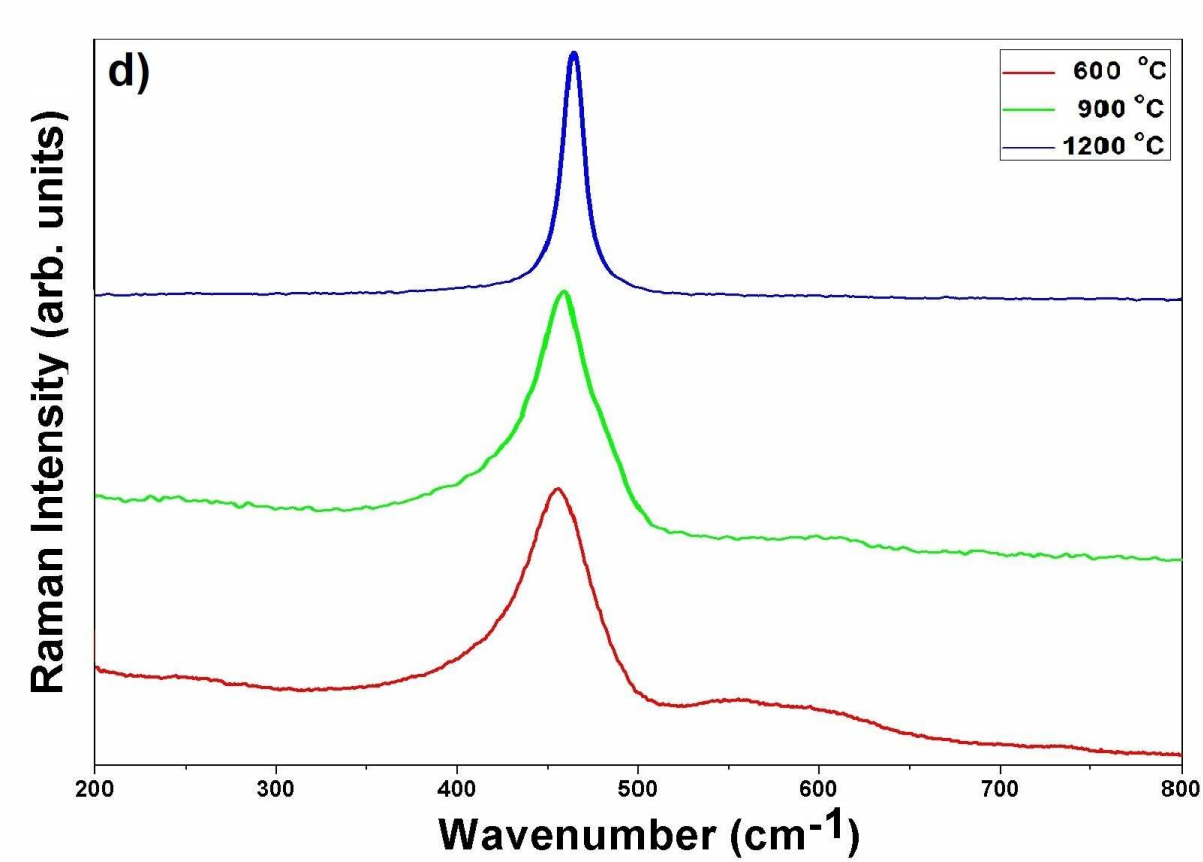

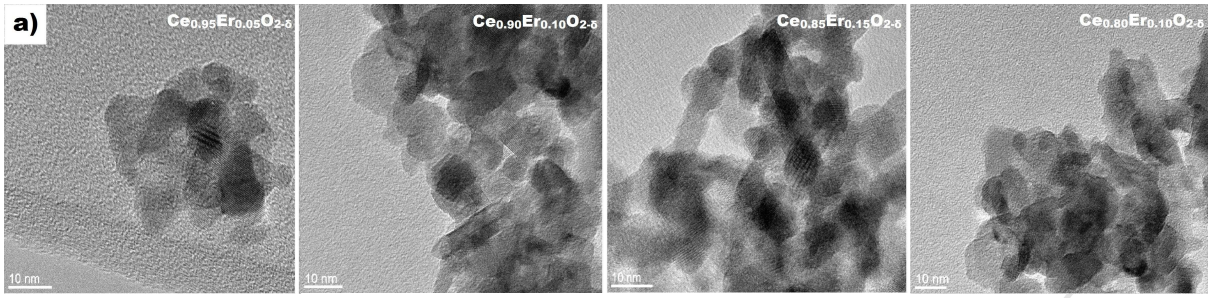

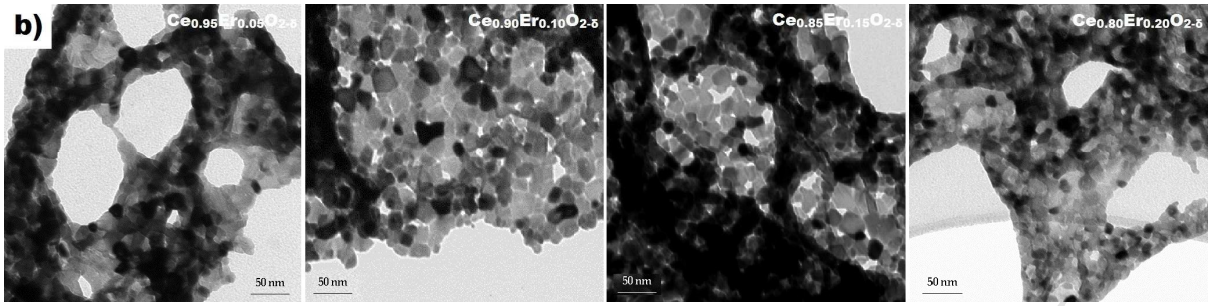

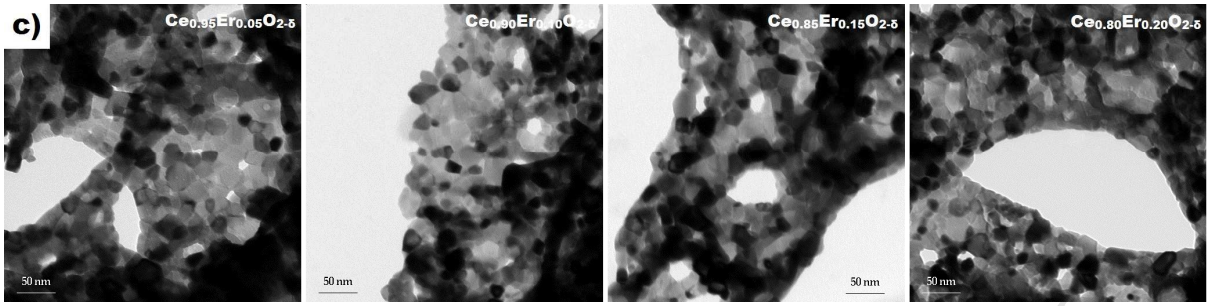

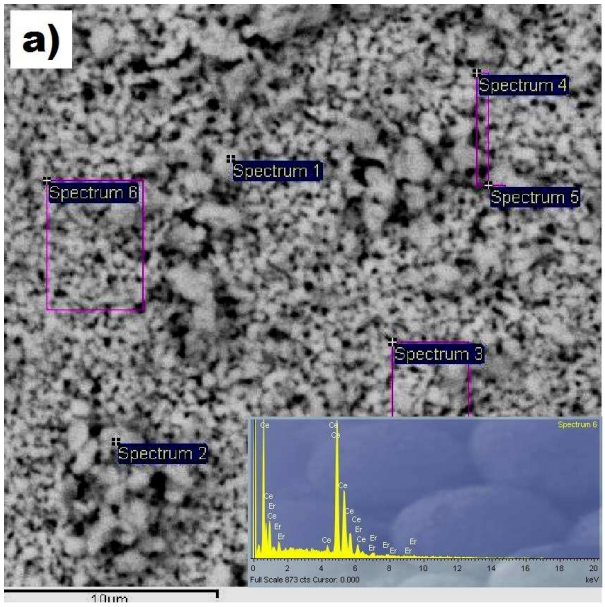

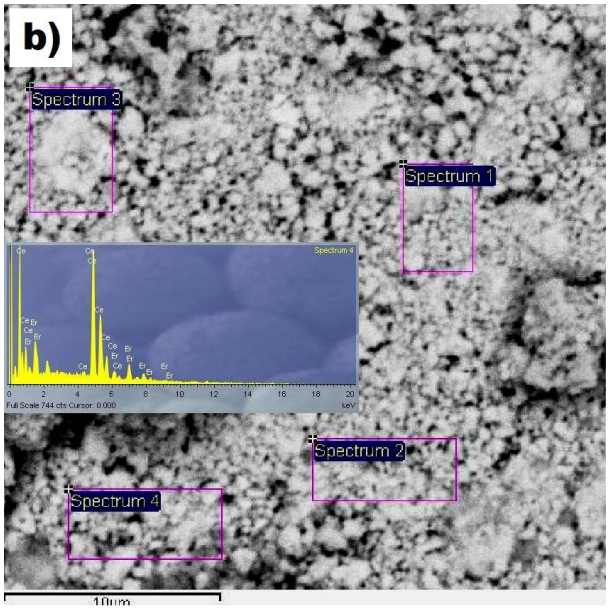

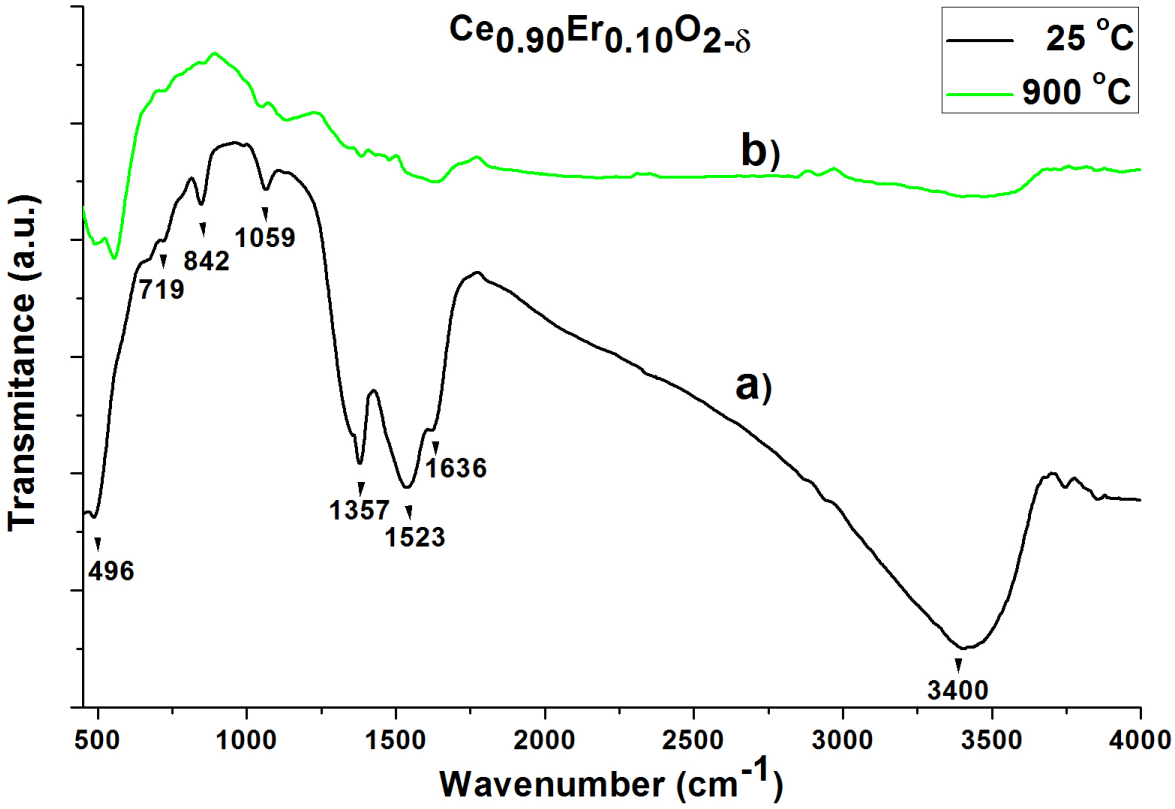

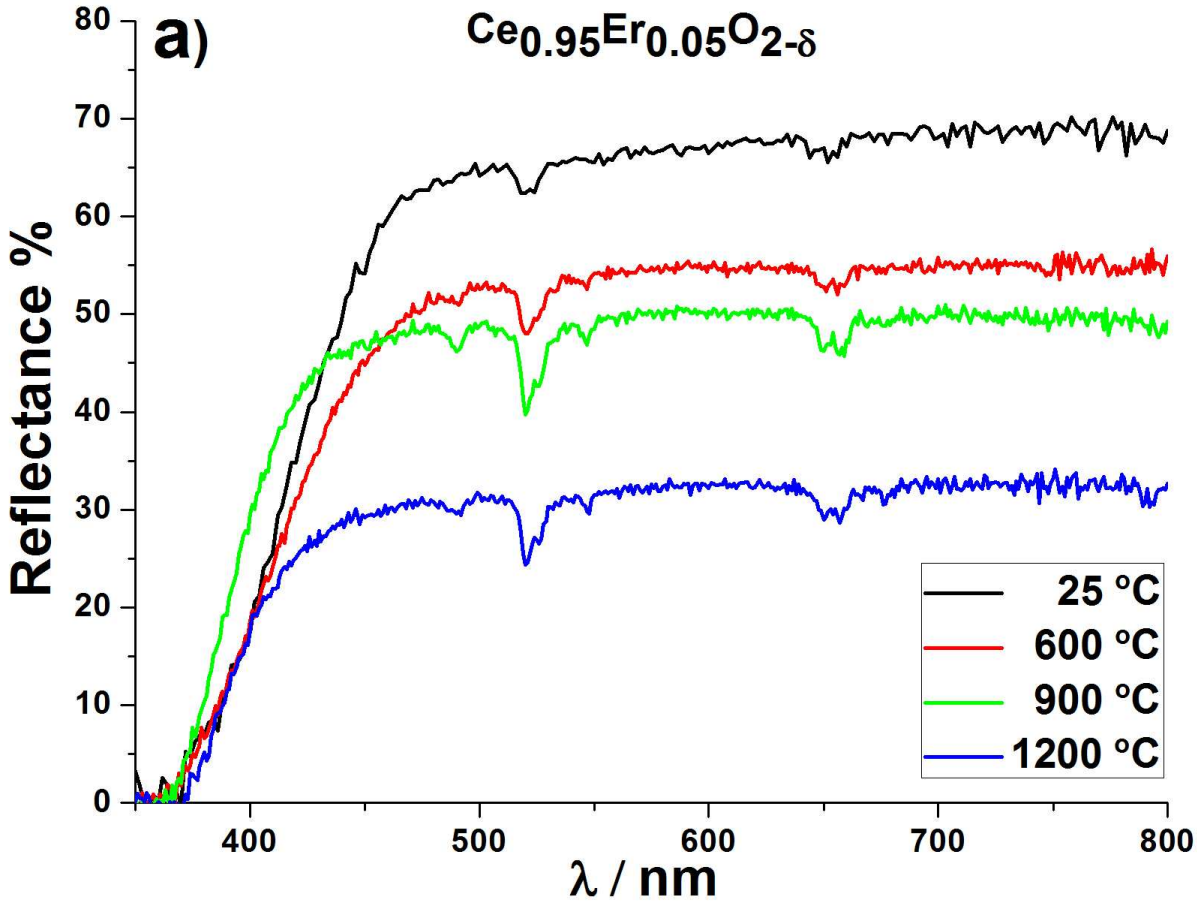

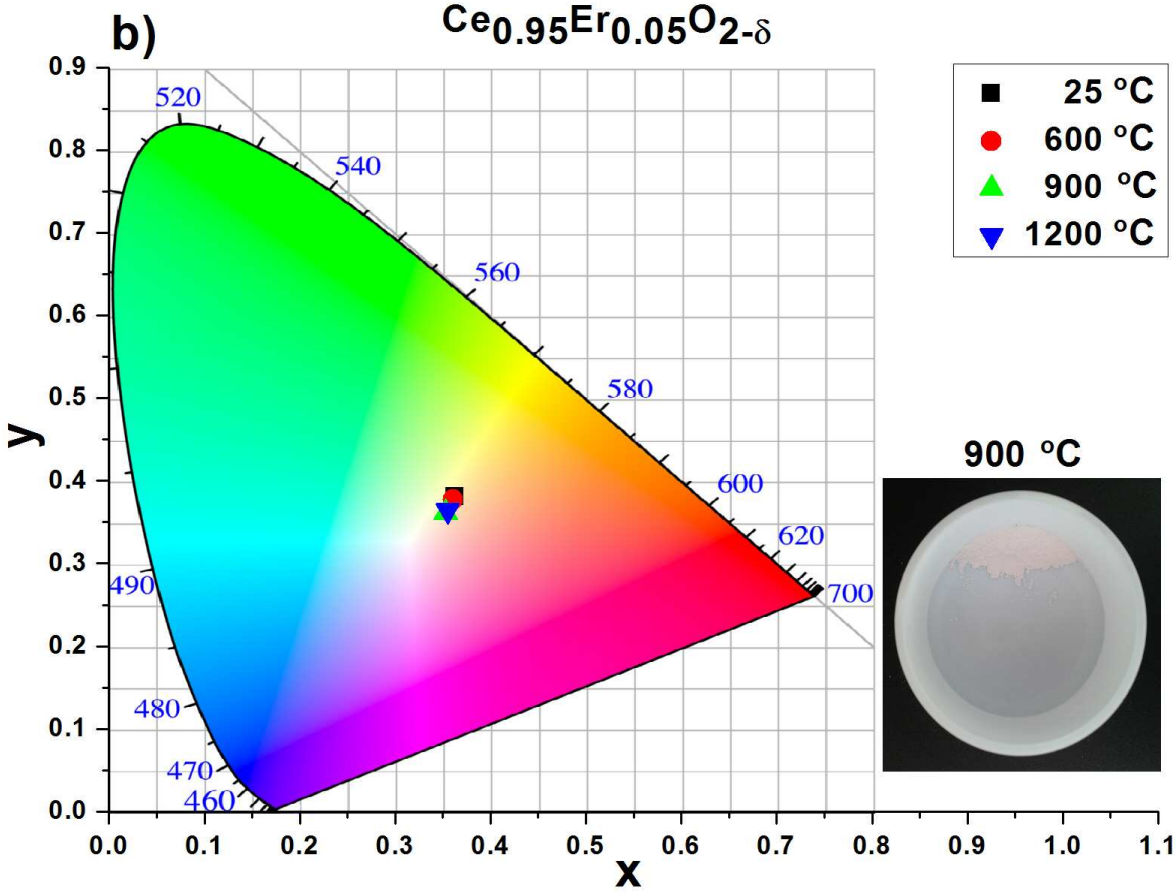

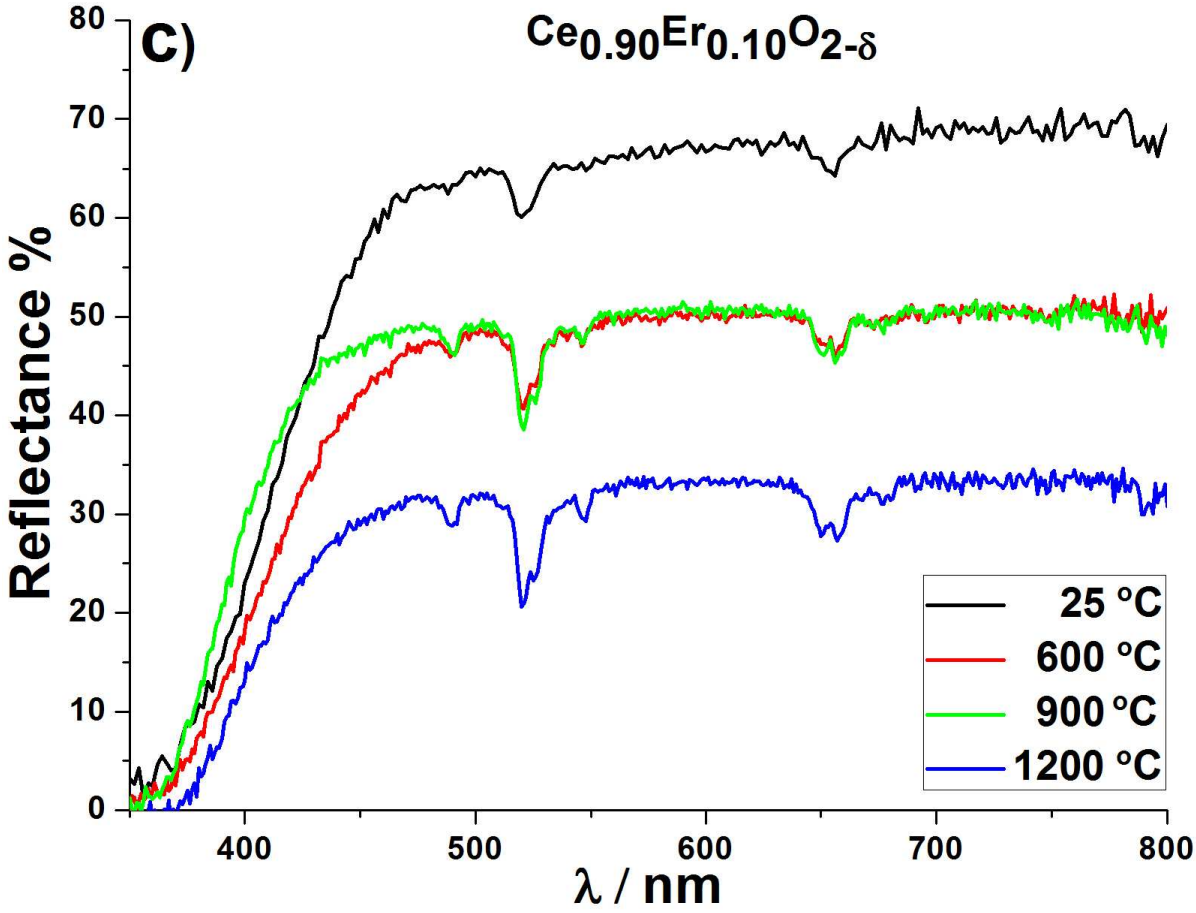

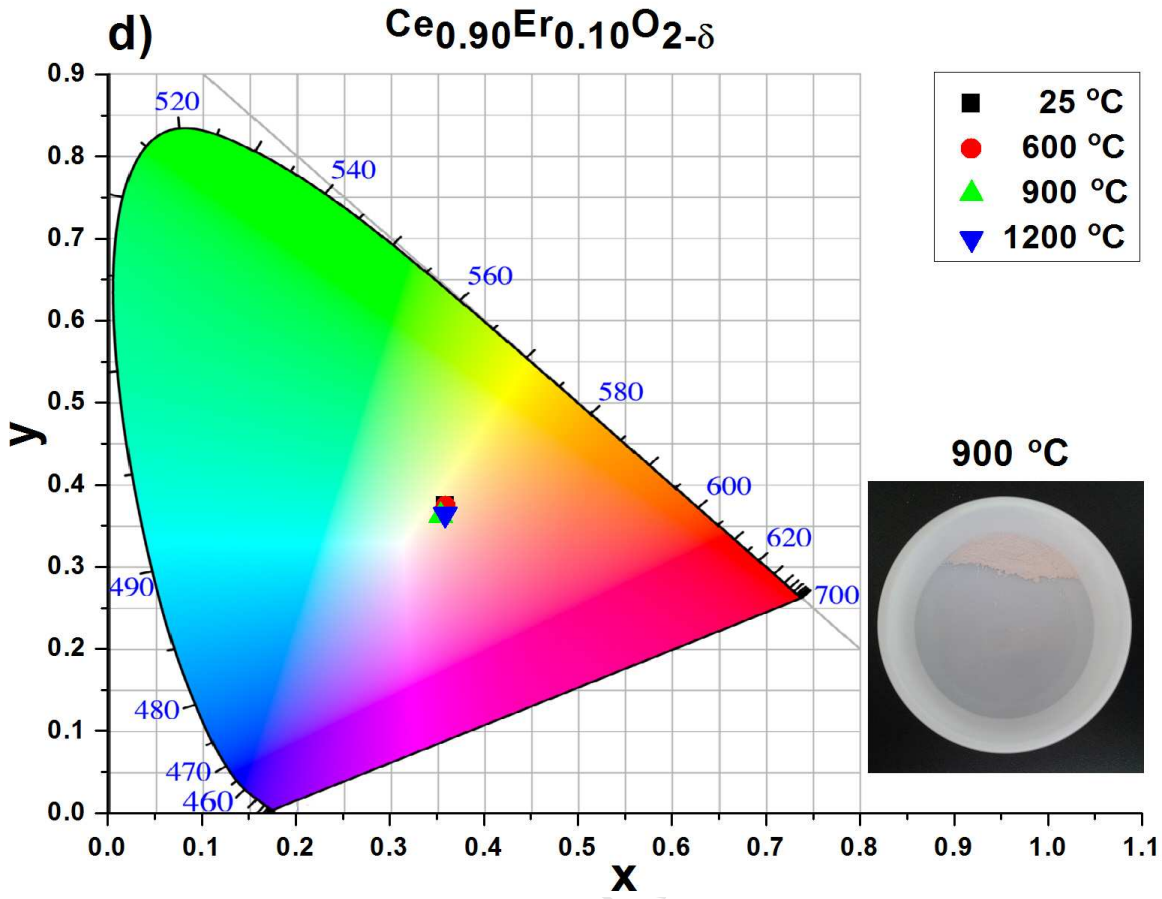

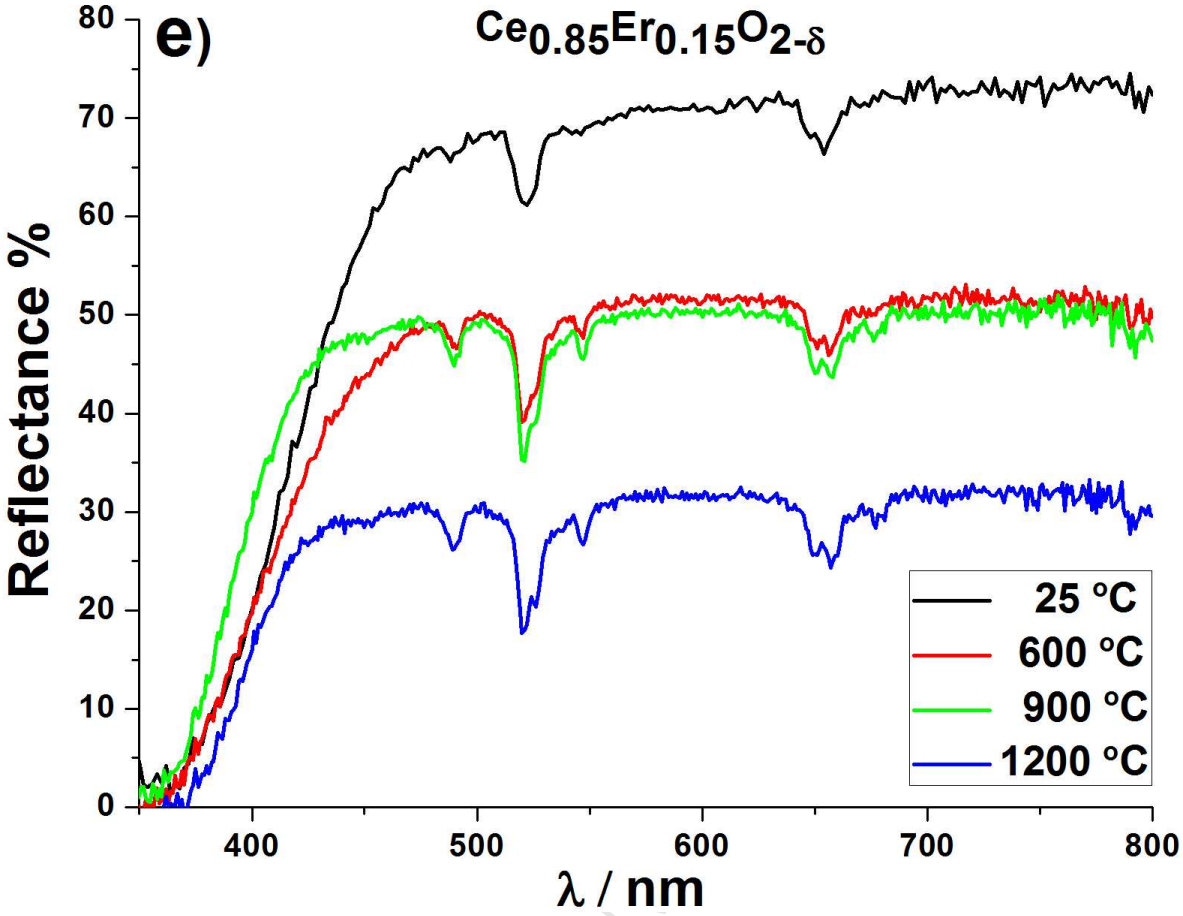

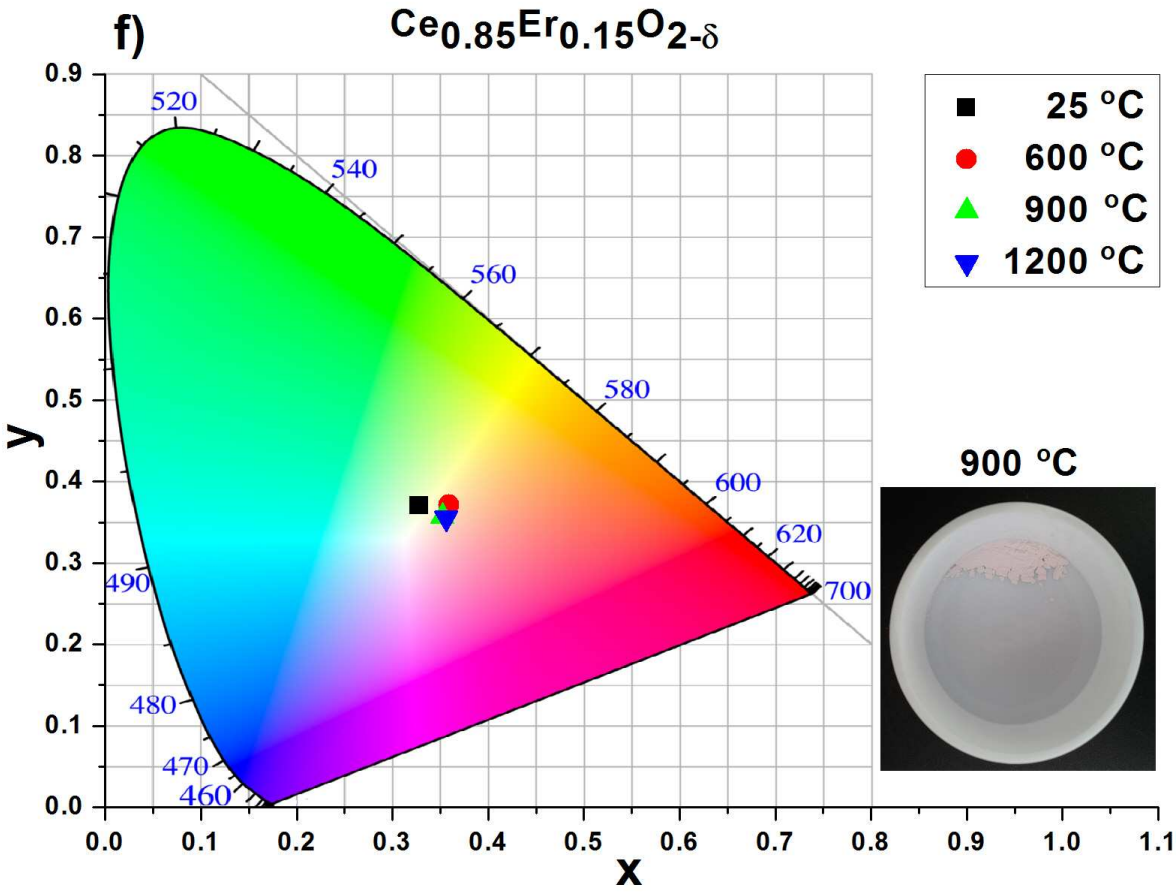

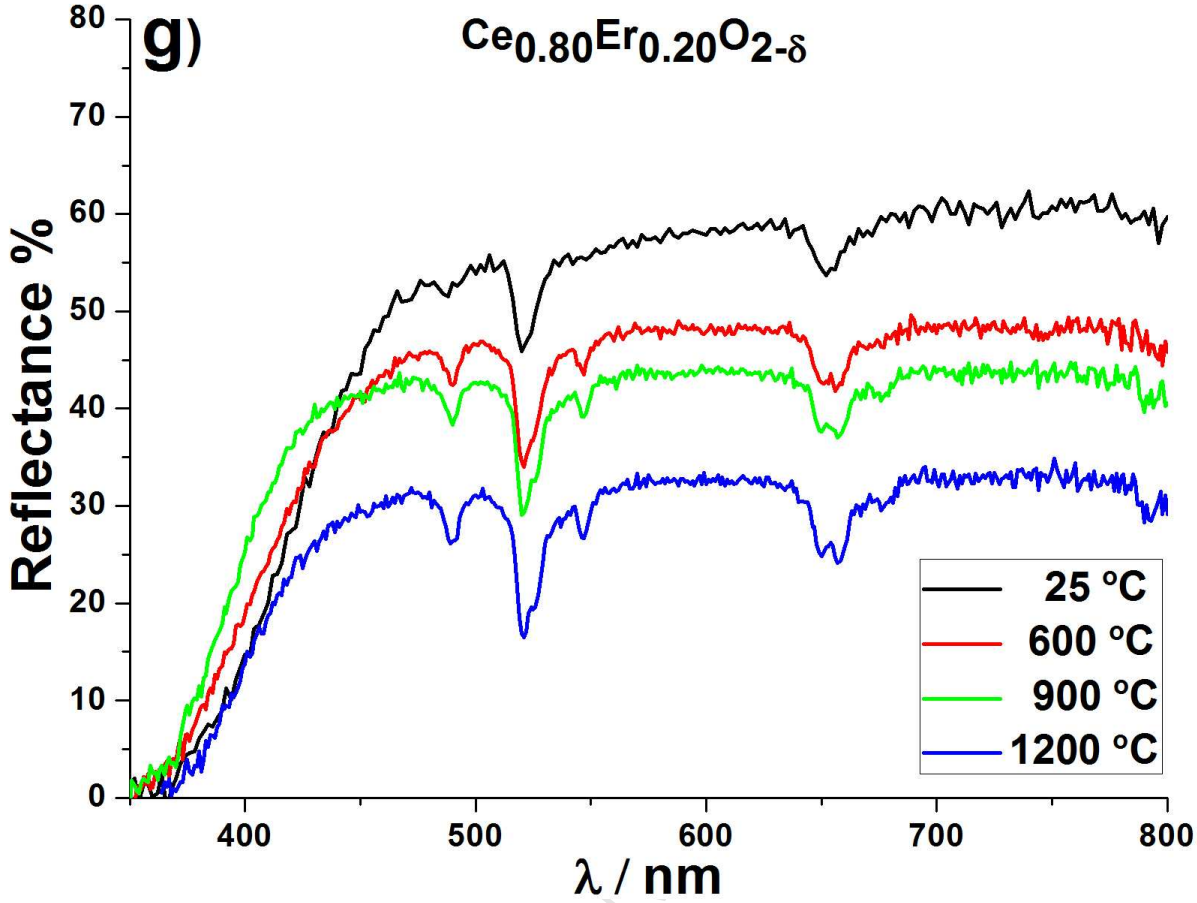

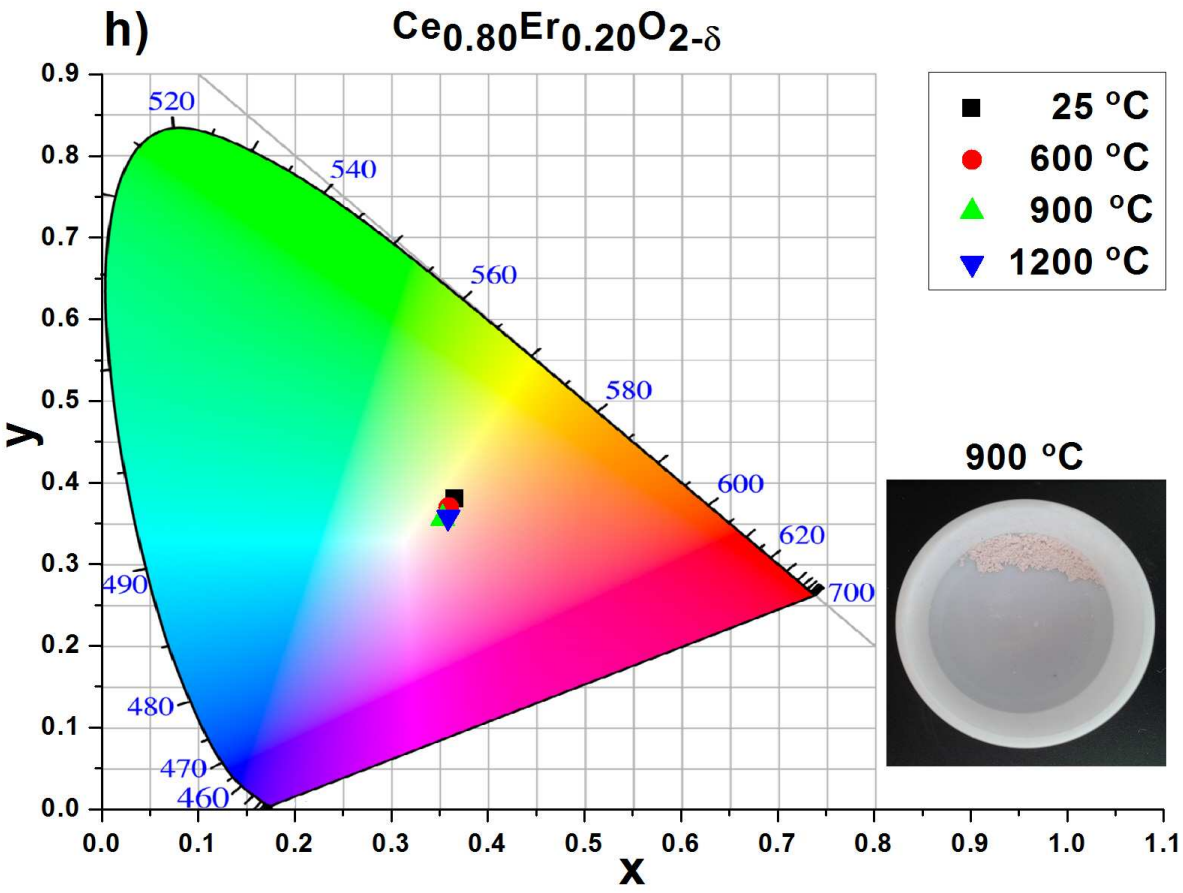

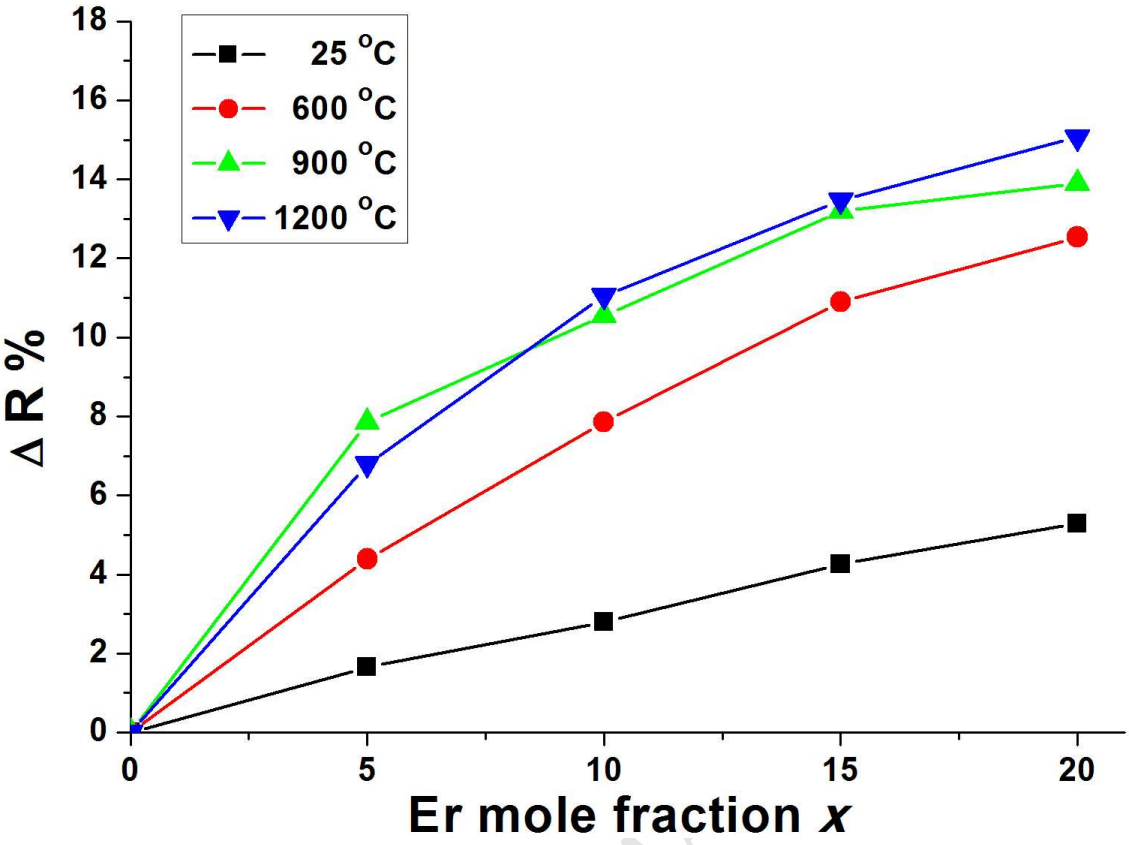

Highlights

1. New inorganic pigments $Ce_{1-x}Er_xO_{2-\delta}$ (x = 0.05–0.20) were prepared by SPRT method.
2. Single–phase form was evidenced for each pigment by XRPD and Raman spectroscopy.
3. The XRPD and TEM analysis showed that the crystallites of nanometric dimensions.
4. The synthesized pigments shows great thermal stability and various pink shades.
5. Pigments may be a potential alternative to the classical toxic pink pigments.